Transparent Conducting Oxides by Atomic Layer Deposition

by

Mari Endresen Alnes

Dissertation presented for the degree of
Philosophiae Doctor (Ph.D.)

Department of Chemistry
Faculty of Mathematics and Natural Sciences
University of Oslo

April 2014

© **Mari Endresen Alnes, 2015**

Series of dissertations submitted to the
Faculty of Mathematics and Natural Sciences, University of Oslo
No. 1618

ISSN 1501-7710

All rights reserved. No part of this publication may be
reproduced or transmitted, in any form or by any means, without permission.

Cover: Hanne Baadsgaard Utigard.
Printed in Norway: AIT Oslo AS.

Produced in co-operation with Akademika Publishing.
The thesis is produced by Akademika Publishing merely in connection with the
thesis defence. Kindly direct all inquiries regarding the thesis to the copyright
holder or the unit which grants the doctorate.

Acknowledgements:

This work has been performed at the Centre for Materials Science and Nanotechnology (SMN) and the Department of Chemistry at the University of Oslo from 2008 to 2015. This work has been part of the project "Conducting Oxides and Nanostructures for Energy technology (CONE)" funded by the Norwegian research council through the NanoMat program (NFR number 181882).

Many thanks to my main supervisor Ola Nilsen for all the help, good discussions and for motivating me to continue even though finalizing a thesis seemed far away when combining work and writing. Already during my first year as a bachelor student my curiosity was intrigued by this technique where molecules were "sprinkled" over a surface and films were built up by an atomic layer at a time! I would also like to thank my co-supervisor Helmer Fjellvåg and Edouard Monakhov for good discussions and useful input.

During all these years at the University of Oslo I have come to know a lot of great people that have contributed to help me with the scientific work and for making the everyday-life at Uni fun and inspiring; Chris, Erik, Hanne, Heidi, Irini, Karina, Knut, Kristin, Laurent, Madeleine, Mareike, Per-Anders, Super-Jon, Titta, Tor and Ville. Thanks also to all of my fellow colleagues and students in the NAFUMA-group, SMN and MiNa laboratory that I have met during these years.

Thanks to my family and friends for always believing in me, and last but not least my boyfriend Mathias for all his support and encouragement.

Abstract

Energy demand and emissions of greenhouse gases are increasing. The use of renewable energy such as solar energy, hydro power and wind power can help mitigate further emissions. Transparent conducting oxides (TCO's) are an important class of materials of relevance for renewable energy. ZnO and SnO_2 are well-known n-type TCO materials that are good candidates to replace the commonly used Sn-doped In_2O_3 (ITO). Delafossite type oxides, Cu*M*O_2, are potential candidates as p-type TCO materials. By realization and combination of n- and p- type transparent oxides into p-n junctions one will enable the fabrication of transparent solar cells and transparent transistors that can lead to functionalization of already available surfaces, such as windows etc.

This study has investigated the deposition of a selection of different materials suitable as TCO's. The selection comprises the materials ZnO, SnO_2, CuO, Cu-Al-O and Cu-Y-O, which has been deposited using Atomic Layer Deposition (ALD). CuO was deposited as a critical step to enable growth of films in the Cu-*M*-O system (*M*=Al/Y).

The work related to deposition of ZnO focused on the purity of the precursors used and whether they were a source for impurities in the resulting film, especially with respect to Al content. It was seen that the precursors might lead to Al doping in the film and that this level might not be easily controlled if the purity grade of the precursor is not sufficiently high. Related to this work, the heterojunction between the film and Si substrate was studied. This is important whenever ZnO is to be used as a transparent electrode for solar cells. It was seen that the junction was improved by annealing the film at 400 ºC.

A process using SnI_4 and O_3 to deposit SnO_2 has been studied at temperatures below 300 ºC in order to investigate the crystal structure, electrical and optical properties of the as-deposited films. The process enables growth from a temperature of 110 ºC. Films deposited at temperatures of 300 ºC are crystalline while at lower temperatures the films are amorphous. UV-vis-NIR spectroscopy shows absorption due the fundamental absorption in the films. For films deposited at 300 ºC the specific resistivity is $7.1 \cdot 10^{-3}$ Ω cm, carrier concentration of $5 \cdot 10^{19}$ cm^{-3} and the mobility is 17 cm^2/V·s. The SnO_2 process has also been used as a buffer layer during high temperature annealing of Cu-Al-O films due to its chemical robustness.

A process to deposit CuO has been studied using copper acetylacetonate, [Cu(acac)$_2$] and O_3. The process was found to give uniform films following the self-limiting growth pattern of ALD in a temperature range of 140 – 230 ºC with a growth rate of ~0.038 nm/cycle. The films were crystalline as deposited with the tenorite structure.

Good control of stoichiometry in the Cu-Al-O and Cu-Y-O systems by combining the processes for deposition of CuO, Al_2O_3 and Y_2O_3 has been achieved. Films with the delafossite type structure were obtained by high temperature annealing of films containing Cu and Al.

The current compilation of work shows that the ALD technique is well suited for deposition of conducting and transparent materials.

Table of Contents

Acknowledgements: i

Abstract iii

Table of Contents v

Glossary ix

List of papers and author’s contribution xi

1 Introduction 1

1.1 Motivation 1

1.2 Scope of work 3

2 Background 4

2.1 Electrical conductivity 4

2.1.1 Doping 7

2.1.2 p-n junction 8

2.2 Optical Properties 9

2.3 Transparent Conducting Oxide 10

2.3.1 Applications and requirements 11

2.4 Atomic Layer Deposition (ALD) 13

2.4.1 The surface utilization concept 15

2.5 Materials 16

2.5.1 ZnO 17

2.5.2 SnO_2 18

2.5.3 Delafossite - $CuMO_2$ 21

3 Characterization methods 27

3.1 X-ray based methods 27
3.1.1 X-ray diffraction (XRD) 27
3.1.2 X-ray reflectometry (XRR) 28
3.1.3 X-ray fluorescence (XRF) 29
3.1.4 X-ray photoelectron spectroscopy (XPS) 29
3.2 Optical spectroscopy 30
3.2.1 Spectroscopic Ellipsometry (SE) 30
3.2.2 UV-VIS-NIR spectroscopy 30
3.3 Electrical Characterization 31
3.3.1 Four-point-probe Measurements 31
3.3.2 Van der Pauw and Hall measurements 32
3.4 Secondary Ion Mass Spectroscopy (SIMS) 33
3.5 Atomic Force Microscopy (AFM) 33
4 Present work – results and discussion 34
4.1 ZnO 34
4.1.1 Diethyl zinc (DEZ) 34
4.1.2 Heterojunction between ZnO and Si(100) and work function of ZnO 35
4.2 SnO_2 37
4.2.1 ALD process 37
4.2.2 Electrical and optical properties of the as-deposited SnO_2 films 40
4.3 Cu-M-O (M=Al and Y) 42
4.3.1 Deposition of CuO 42
4.3.2 Deposition of Cu-Al-O and Cu-Y-O films 44
4.3.3 $CuAlO_2$ 49
4.3.4 Cu-Y-O 50
5 Concluding remarks and future work 52

6 References 54

Glossary

AALD	atmospheric atomic layer deposition
AFM	atomic force microscopy
ALD	atomic layer deposition
AMLCD	active matrix liquid crystal display
AZO	Al-doped zinc oxide
CVD	chemical vapor deposition
DEZ	diethyl zinc
EJ	10^{18} joule or exajoule
FTO	F-doped tin oxide
IR	infra-red
ITO	indium tin oxide
NIR	near infra-red (light)
PEALD	plasma enhanced atomic layer deposition
PLD	pulsed laser deposition
PV	photovoltaic
Rms	root mean square
SE	spectroscopic ellipsometry
SIMS	secondary ion mass spectroscopy
SXRD	synchrotron X-ray diffraction
TC	transparent conductor
TCO	transparent conducting oxide
TEM	transmission electron microscopy
TFT	thin film transistor
TFTLCD	thin film transistor liquid crystal display
TMA	trimethyl aluminum
TTFT	transparent thin film transistor
UV	ultra violet
UV-vis	ultra violet – visible (referred to light)
XPS	X-ray photoelectron spectroscopy
XRF	X-ray fluorescence spectroscopy
ZTO	Zinc tin oxide

List of papers and author's contribution

I **Atomic Layer Deposition of Copper Oxide using Copper(II) Acetylacetonate and Ozone**
Mari Endresen Alnes, Edouard Monakhov, Helmer Fjellvåg and Ola Nilsen
Published in Chemical Vapor Deposition, Volume 18, Issue 4-6, Pages 173-178, June 2012

The author planned and executed all experiments with the exception of the XPS measurements. The author was heavily involved in the interpretation of the data and wrote the manuscript, organized the writing process and finalized the manuscript for submission.

II **Atomic layer deposition of SnO_2 at low temperatures using SnI_4 and O_3**
M. Alnes, H. Beckstrøm, P. A. Hansen, J. E. Bratvold, E. Monakhov, H. Fjellvåg, O. Nilsen
Manuscript ready for submission

The author planned all experiments. The author executed all experiments with the exception of the depositions, UV-vis-NIR and ellipsometry measurements. The author was heavily involved in the interpretation of the data and wrote the manuscript, organized the writing process and finalized the manuscript for submission.

III **Growth of Cu-*M*-O materials (*M* = Al/Y) using atomic layer deposition (ALD)**
M. Alnes, E. Østreng, E. Monakhov, H. Fjellvåg and O. Nilsen
Submitted to Dalton Transactions

The author planned and executed all experiments with the exception of the SXRD measurements. The author was heavily involved in the interpretation of the data and wrote the manuscript, organized the writing process and finalized the manuscript for submission.

Additional papers that is related to thesis but not included

Electronic Properties of ZnO/Si Heterojunction Prepared by ALD
Vincent Quemener, Mari Alnes, Lasse Vines, Ola Nilsen, Helmer Fjellvåg, Eduard Monakhov, Bengt Svensson
Published in Solid State Phenomena, Volume 178-179, Issue Gettering and Defect Engineering in Semiconductor Technology XIV, Pages 130-135, 2011

The work function of n-ZnO deduced from heterojunctions with Si prepared by ALD
Vincent Quemener, Mari Alnes, Lasse Vines, Protima Rauwel, Ola Nilsen, Helmer Fjellvåg, Eduard Monakhov, Bengt Svensson
Published in Journal of Physics D: Applied Physics, Volume 45, Issue 31, Pages 315101, 2012

1 Introduction

The use of fossil fuels is continuously increasing due to population growth and emerging economies, bringing with it emission of greenhouse gases[1]. There is already a consensus in the scientific community that the amount of greenhouse gases has already led to climate change. Warming is unequivocal, human influence on the climate system is clear and continued greenhouse gas emissions will lead to further climate changes[2]. Efforts to mitigate the emission of greenhouse gases are inevitable in order to prevent further climate change. Utilizing renewable energy sources such as solar energy, wind- and hydro power and bio-fuels are some of the measures that can mitigate the emission of greenhouse gases.

This work has focused on deposition of metal oxides as materials for transparent conducting oxides (TCO's). TCO's are an important class of materials within renewable energy applications and can enhance the efficiency of traditional solar cells as well as enable design of new types of transparent electronics. TCO's can also be used to functionalize windows to reduce emission of heat or to produce electricity.

1.1 Motivation

In 2010 66.6% of the electricity production in the world came from fossil fuels according to *"The World fact book"*[3]. There are many available solutions today that can help mitigate the greenhouse gas emissions. Good technological solutions to utilize the earth's renewable energy resources exist. Solar radiation is one of the most important renewable energy resources. The technical potential of the annual solar irradiation is 3 – 100 (3 represents the minimum estimation and 100 the maximum)[4].times the primary energy consumption in 2008. The technical potential is calculated based on practical availability of land, realistic conversion efficiencies, annual clear-sky irradiation and sky clearance. The technical potential for the solar irradiation to Earth might seem low since Earth's surface receive about 8000 times more energy per year from solar irradiation than the primary energy consumption in 2008. However, to utilize this energy the radiation to all of Earth's surfaces (land and ocean) would have to be harnessed with a 100 % conversion efficiency[5].

Direct solar energy technologies harness the energy of solar irradiance to produce electricity, thermal energy (heating or cooling), to meet direct lighting needs and potentially to be used to produce fuels. The technology for producing fuels by solar energy is still immature, whereas concentrated solar power (CSP) solutions to produce electric power is emerging. The most mature technologies utilizing solar irradiation is the thermal power systems for heating and cooling and the wafer based photovoltaics for electric power generation[6].

There is a huge potential within utilizing the waste solar energy resource. Even though the research within photovoltaics is mature there are still opportunities to improve the technology to meet with the public demand. Higher efficiencies, lower costs, implementation of non-toxic and abundant materials as replacement of some of the present expensive and toxic materials (In, Cd), will improve the technology and its implementation further [7-10].

Cost reduction for the renewable energy applications can be achieved by cheaper, faster and larger scale production processes. Governmental incentives are also beneficial for increasing the use of renewables.

The efficiency of present solar cells can be increased by utilizing more of the solar irradiation. Introduction of transparent front contacts on solar cells will increase the active surface area by limiting shading from metal front contacts. However, the present progress is limited by development of new transparent conducting materials based on abundant materials. A progress in this field will also be important for the electronics market as all flat panel displays rely on transparent conducting oxides. The need for transparent electronics is driven by the real-estate principle for utilizing already existing surfaces[11]. Windows can be used for electricity production or be functionalized with respect to light shielding and in realizing transparent thin film transistors (TTFT's). Transparent solar cells have lower efficiencies than conventional wafer based photovoltaics. Due to the fact that the solar cells are transparent, most of the solar irradiation will be transmitted or reflected, while only the shorter wavelengths will be absorbed to produce electricity. However, functionalizing the vast amount of glass in buildings, such as skyscrapers and office buildings, offer a good potential for transparent solar cells.

1.2 Scope of work

N-type TCO materials are important as transparent electrodes for renewable energy applications such as front contacts which increase the efficiency of solar cells as well as within transparent electronics. Finding a good p-type TCO will lead to the realization of transparent p-n junction (see chapter 2.1.2) which can be used as transparent solar cells on windows, transparent transistors and other transparent electronic gadgets so far only seen in the Sci Fi movies.

This work has mainly focused on three materials, namely zinc oxide (ZnO), tin(IV) oxide (SnO_2) and copper aluminum oxide ($CuAlO_2$). ZnO and SnO_2 are well known n-type TCO materials. $CuAlO_2$ is a potential candidate as a p-type TCO material. Thin films of the materials have been prepared using Atomic Layer Deposition (ALD). The contribution of this work has been to gain more knowledge for already known processes, and to find new routes to deposit the materials, which has been done for CuO deposition.

2 Background

Materials can be classified according to many different systems, one is to relate the classification to their electrical properties and divide them into metals, semiconductors or insulators. Metals are normally good conductors, while the conductivity of semiconductors is strongly related to their doping levels. Insulators do not conduct electricity. The reason for the differences in conductivity is mainly due the materials band gap. Band gap is the gap between the valence band (highest occupied) and conduction band (lowest unoccupied) in a material. See an illustration of the band gaps for metal, semiconductor and insulator in Fig 1. The band gap for insulating materials is generally so large that they become optically transparent for visible light. How is it then possible to have a transparent material that can conduct electricity?

This chapter will first introduce the two most important properties for TCO materials, namely; optical transparency and electrical conductivity. Based on this, some of the applications utilizing TCO materials and their requirements will be mentioned. The thin film technique used in this study, ALD, will be presented briefly before the materials studied in this work will be presented.

2.1 Electrical conductivity

Electrical conductivity is a measure of a materials ability to transport (conduct) an electric current. In this part the focus will mainly be on electrical conductivity in semiconductors.

Atoms are built up of a positive core with electrons distributed around in orbitals. This gives discrete energy levels in the atom where the electrons are allowed to be. When atoms are "put together" chemical bonds are formed. The atomic orbitals are then transformed into molecular orbitals where the number of discrete levels relates to the number of atoms taking part in the molecule. The extension of this is that for structured solid materials, the number of levels becomes so large that they appear as energy bands. The transport/conductivity of electrons (and holes) in a material are determined by these energy bands. Such bands are shown in Fig 1. For metals, the valence band is only partly filled

and the electrons can easily move. For ideal semiconductors and insulators, the valence- and conduction band is separated by a band gap leaving the valence band completely filled and the conduction band empty. A completely filled band cannot conduct electricity since the mobility of the electrons will be zero because they do not have any vacant position to move into. For a semiconductor, the gap is small enough so that electrons can be exited to the conduction band by absorption of visible light or by absorption of thermal energy. In the excited state, the mobility will increase both in the conduction and valence band, and hence semiconductors become electronically active. Semiconductors can be converted into permanently electronically active materials by doping, a process that will be described in chapter 2.1.1. A material is transparent to visible light if the band gap is higher than ~3 eV[12]. The band gap of insulating materials is so large that the magnitude of excited electrons becomes negligible. As an example, the band gap in SiO_2 is 9 eV. However, there is no clear definite limit separating semiconductors from insulators. The conductivity of a material can therefore be used to define whether it is an insulator or semiconductor. This is because the conductivity can be enhanced by doping[13], making the band gap no certain measure for the materials conductivity.

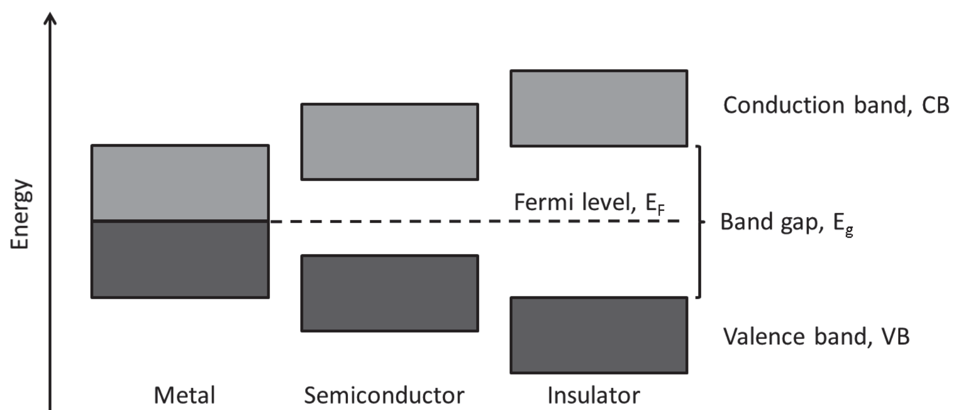

Fig 1 A comparison of the band gaps of metals, insulators and semiconductors.

The band structure in a material is not as simple as presented in Fig 1. The band structures reflect the periodic arrangement of atoms in crystalline structures and become dependent on the direction in the material. Fig. 2 shows the band structure diagram for tin(IV) oxide and silicon.

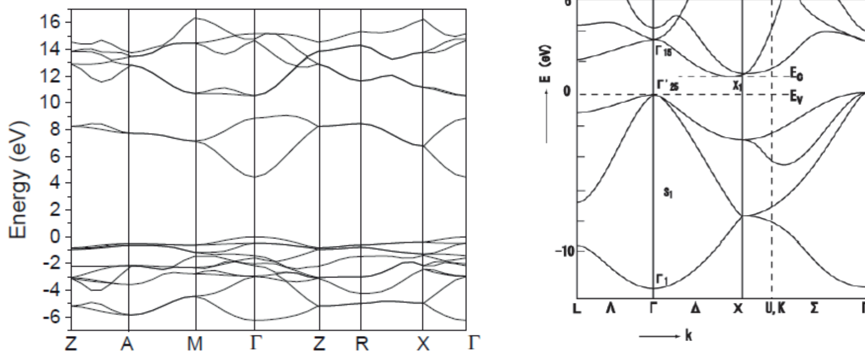

Fig 2 Band structure of the direct band gap material SnO_2 (left) and the indirect band gap material Si (right), pictures adapted from Ref[14] and Ref[15] respectively.

The band structure diagram shows the energy bands in the material. The bands are separated by the band gap. The letters along the x-axis (Γ, M, Δ etc.) are directions in the crystalline material[16, 17]. If the minimum of the conduction band lies at the same position as the maximum of the valence band, the material is a direct band gap semiconductor. The alternative is an indirect band gap where the electron will have to alter its momentum while being excited. This will influence how an electron is relaxed from its exited state in the conduction band to the valence band. In semiconductor light emitting devices direct semiconductors are normally chosen. Exited electrons will recombine directly with a hole in the valence band and emit light. The probability of light being emitted from recombination of excited electrons in an indirect semiconductor is small. Recombination for excited electrons in an indirect band gap follows recombination with impurity/defect energy levels within the band gap. This will emit heat to the lattice.

The conductivity, σ, of a material is given by equation 2.1.

$$\sigma = qn\mu \tag{2.1}$$

Where q is the electron charge, n the carrier concentration and μ the mobility. In semiconductors, both electrons and holes are carriers and both will contribute to the conductivity. Then equation 2.1 will be written as equation 2.2.

$$\sigma = nq\mu_n + pq\mu_p \tag{2.2}$$

Where p is the carrier concentration of holes. The mobility μ is defined as:

$$\mu_{e/h} = \frac{e\tau}{m^*_{e/h}} \tag{2.3}$$

τ is the average time an electron spends between two successive scattering events and $m^*_{e/h}$ is the effective mass. Sources for scattering could be phonons, impurities, defects and dopants.

2.1.1 Doping

In order for an electron to move in an applied electric field, there must be allowed unoccupied energy states for it to move to. A semiconductor where no dopant is present is called an intrinsic semiconductor. If an electron is excited to the conduction band it will leave a hole in the valence band. The concentration of holes and electrons will be the same. If a semiconductor is doped it is called extrinsic. It will then be either n- or p-type, meaning a higher concentration of either electrons (n-type) or holes (p-type). Dopants introduce new energy states within the band gap. Dopants with excess electrons can donate these to the conduction band. The material will then have an excess of electrons (n-type), and the material is donor doped. If a dopant that is electron deficient is introduced, it can accept an electron from the valence band. The material will then have an excess of holes (p-type). A donor dopant should introduce an energy level close to the conduction band. This will ensure that only a small amount of energy is required to excite/donate the excess electron to the conduction band. If the energy level introduced by the donor dopant is close to the conduction band it is called a shallow donor. If the donor introduces an energy level further away from the conduction band it is called a deep donor. Acceptor dopants should introduce an energy state right above the valence band, so that electrons easily can be exited to the energy level introduced by the acceptor dopant. Note; some metal oxides are referred to as intrinsic n- or p-type materials, this means that it normally forms native defects, such as vacancies and interstitials, that act as dopants even though no foreign dopant is present in the material.

The distribution of electrons between the valence and conduction band follow the Fermi-Dirac distribution. The Fermi level is where the probability of finding an occupied electron state is ½. For intrinsic semiconductors the Fermi level lies in the middle of the band gap as shown in Fig 1, while it is shifted either towards the valence- or conduction band depending on whether the material is p- or n-type, see Fig 3. If a semiconductor is doped heavily n-type the dopants come closer together and can no longer be considered to have discrete energy levels. They will form energy bands that can overlap with the bottom of the conduction band. If the concentration of conduction band electrons is higher than the effective densities of states, the Fermi level will no longer lie in the band gap, but will be in the conduction band. The material is then a degenerate semiconductor. A degenerate p-type doped semiconductor will have the Fermi level in the valence band.

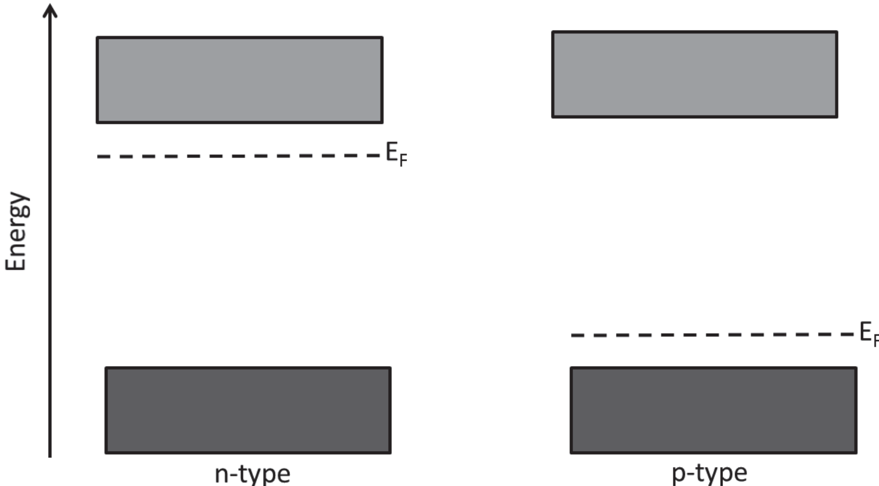

Fig 3 Band gap structure extrinsic (n and p). Fermi level, E_F, indicated

2.1.2 p-n junction

When a p- and n-type semiconductor are joined together they form a p-n junction. The p-n junction is essential for the operation of devices such as; solar cells, some transistors and diodes. A p-n junction is illustrated in Fig 4. When the n- and p-type semiconductor are brought together electrons will move towards the p-side and holes will move towards the n-side. This is called the depletion zone which acts as a barrier for further transport of carriers. If an external voltage is applied, it can either give rise to a forward- or reverse bias

that will change the "size" of the depletion zone. It can either make the junction conduct better or make it into an insulator. This is the rectifying character of a p-n junction. If light with energy higher than the band gap is shone on the junction, an electron-hole pair will be created. The junction separates them so that they will not recombine but rather be used in an electric circuit. This is the construction of a solar cell.

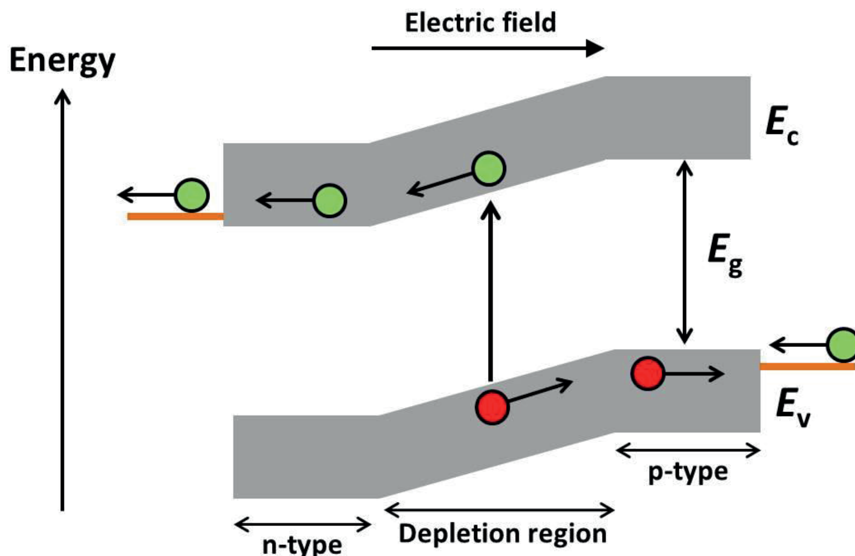

Fig 4 P-n junction. An illustration showing an electron (green sphere) being excited from the valence band to the conduction band. The electron is then pulled towards the n-type region and the hole (red sphere) is pulled towards the p-type region. Picture is reprinted with permission from Ref. [18].

2.2 Optical Properties

When a photon (light) impinges on the surface of a material, several interactions can occur. It can be reflected from the surface. If it is not reflected it can be absorbed by the material. If the photon is not reflected or absorbed it will be transmitted. When the light travels through the material its path can be changed, or the speed of the light changes, this is called refraction. The light can also be scattered due to internal surfaces etc. inside the material. All these properties are dependent on the energy/wavelength of the photon irradiated on to the material. The changes light undergoes when interacting with a particular substance are known as the optical properties of that substance.

There are many reasons why a material absorbs light. The main cause for absorption of visible light in a solid material is due to the materials band gap. If the photon energy is equal or higher than the band gap of the material it can be absorbed. Typical absorption in a TCO material is described in the next chapter.

2.3 Transparent Conducting Oxide

In the beginning of chapter 2 we asked how it is possible to have a transparent material to conduct electrons. A material having a band gap higher than 3,1 eV (400 nm) is transparent and is called a wide band gap semiconductor. By doping a wide band gap semiconductor the conducting properties will be enhanced. The resulting material is a transparent conductor (TC). Fig 5 shows a typical optical spectra for a TCO material, here it is a ZnO film deposited on glass.

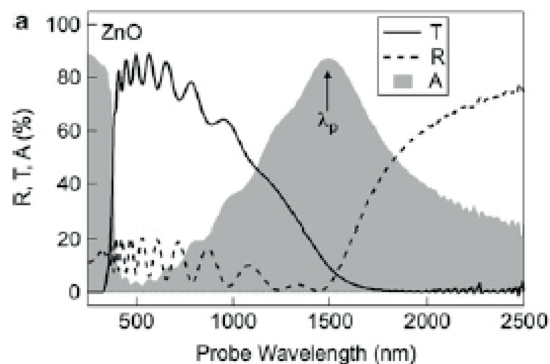

Fig 5 Optical spectra of typical (ZnO) transparent conductor (TC). The figure shows the transmittance (T), absorbance (A) and the reflectance (R). Picture adapted from Ref [19].

The film has a transparency of ~80% in the visible region (400-700nm). Oscillations from thin film interference can be seen for both the transmittance and reflectance in this area. The transmittance cut-off at around 300 nm is due to the fundamental absorption (optical band gap) of the material where electrons are excited from the valence band to the conduction band. The decrease in transmittance and increase in reflectance at higher wavelengths is due to collective oscillation of electrons in the conduction band called plasma oscillations (plasmons). This can also lead to substantial absorption for longer wavelengths as seen in Fig 5. The maximum absorption wavelength due to plasmons is

dependent on the number of electrons in the conduction band (carrier concentration) and will shift towards lower wavelengths when the carrier concentration is increased.

The majority of the TCO's discovered so far are n-type conductors, while only a few p-type conductors are known. Attempts to convert native n-type TCO materials to p-type by heavy doping have been attempted with little success. Going from p- to n-type is also difficult for some of the materials. The reason for this is the formation of defects that compensate the doping. This is why p-type doping of ZnO and n-type doping of $CuAlO_2$ has proven to be difficult, whereas $CuInO_2$ can be both p- and n-doped[19, 20]. Based on the examples above it is seen that there are several factors that needs to be taken into account when finding and designing the right TCO for the desired application.

2.3.1 Applications and requirements

TCO materials are used in many applications and as new materials and improvements are discovered, we might find ourselves with the funny gadgets normally seen in the Sci Fi movies. Some divide transparent conducting (TC) materials into active or passive, based on the TC's role[11]. The passive absorbs energy and could be a simple coating for electrical conductivity or optical purposes such as touch displays, front contacts, solar cells, heating, low e-windows and electro-chromic windows, while the active role is when it is used to control energy flow, as in thin film transistors (TFT's) for use in thin film transistor liquid crystal displays (TFTLCD) and active matrix liquid crystal display (AMLCD). If good p-type TCO's are realized, transparent p-n junctions can be made. In Fig 6 some applications that utilize TCO materials are shown.

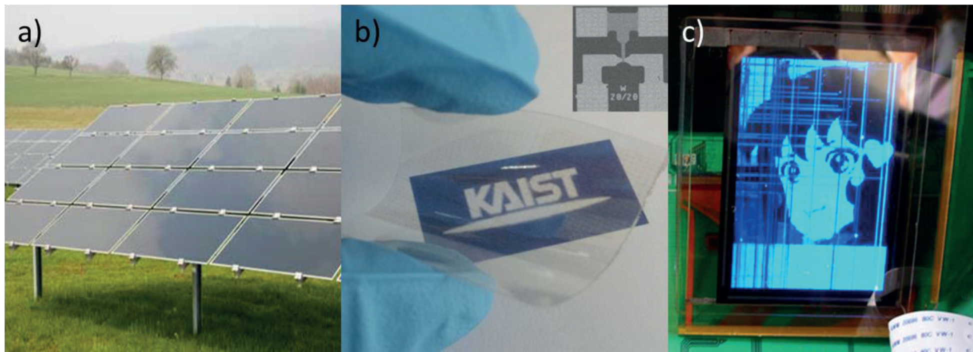

Fig 6 Applications that utilize TCO's: a) Transparent front contact on solar cell array[21] b) a picture of flexible F-doped indium zinc oxide on a PEN film substrate (Insertion picture is an SEM image of the channel region)[22] c) transparent active matrix OLED display with ZnO-based TFTs[23].

Depending on the application there are different requirements for the TCO materials. For transparent electrodes the material should have a carrier concentration of about 10^{20} – 10^{21} cm^{-3} and a resistivity of about 10^{-3} Ω cm or lower. The band gap should be higher than 3 eV and the average transmittance should be higher than 80% for the visible range of the electromagnetic spectrum[12]. As mentioned earlier, absorption due to free carriers is shifted to shorter wavelengths when the carrier concentration is increased. The material might then block some of the useful incoming solar light if it is used as an electrode for a solar cell that can utilize this part of the incoming light. If the TCO material is to be used as the active channel material in a TFT, the carrier concentration should be low, but the material should have a high carrier mobility in the order of ~10-40 $cm^2/V\ s$[19]. Another important point is that the fabrication of the thin film TCO materials should be quick, applicable on large areas and at temperatures below 200 ºC[12]. For TCO electrode materials the thickness should also be less than 200 nm[12].

The industry standard today is indium tin oxide (Sn-doped In_2O_3, ITO). ITO is used in touch screens, flat panel displays and solar cells[8, 12, 19, 24]. The scarcity and limited availability of indium has led to drastically increasing prices of indium the last few years[7-10]. There are readily good candidates such as doped tin oxide and zinc oxide with comparable electrical and optical properties to ITO[12, 19, 24]. One of the reasons why ITO has not been replaced by other TC materials is due to how the material is fabricated and also how easy the material is to etch. Tin(IV) oxide is known to be a highly stable material used

in corrosive environments, while zinc oxide is easily etched[7]. Another aspect is that the display industry has invested heavily in ITO optimized systems and can afford the high price of indium. Other markets such as the photovoltaic industry are more vulnerable to the price of indium[8, 10].

2.4 Atomic Layer Deposition (ALD)

Atomic layer deposition (ALD) is a chemical vapor deposition technique based on self-limiting reactions between gas phase reactants and active sites on a surface. The reactants, called precursors, used to deposit the film are separated from each other by purge steps with inert gas so that they can only react with the surface. The process to create one layer of material with ALD is called an ALD cycle. Fig 7 shows a schematic presentation of one ALD-cycle. For a binary compound such as Al_2O_3, two precursors are used and the cycle consists of four steps. For the deposition of Al_2O_3, trimethylaluminum (TMA) and water (H_2O) are the most used precursors [25, 26].

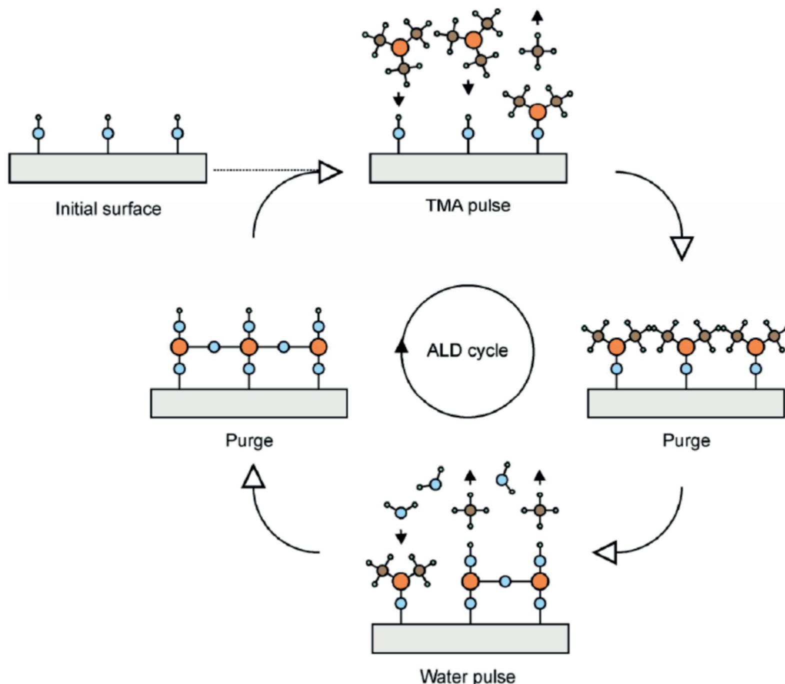

Fig 7 ALD-cycle. See explanation in text. Picture is reprinted with permission from Ref.[27].

The first ALD-cycle starts with the surface of the substrate, often a silicon wafer or soda-lime glass is used as substrate, but the material and structure of it depends on the application[25]. Every surface is terminated by active surface species (-OH groups is a typical surface species) where the precursor can react. In step 1) TMA is pulsed in to the reaction chamber. Here it will react with the active surface species (chemical absorption) available, both on the substrate and the reaction chamber walls. Excess TMA and by-products from the surface reaction should not react. When the surface is saturated, the excess TMA and by-products are purged away in step 2) using an inert gas such as nitrogen (N_2). There will now be one monolayer of reacted TMA on all surfaces. In step 3) water is pulsed in to the chamber and will react with the TMA on the surfaces, creating one Al-O layer. Excess water is purged away in step 4). The cycle can now be repeated until the right thickness is obtained. This controlled reaction cycle is the most important benefit of ALD.

The good thickness control and surface reactions leads to conformal, pin-hole free films that can be deposited on complex surfaces. The use of metal organic and organometallic precursors leads to low deposition temperatures. The temperature range for a specific precursor system where ALD growth is obtained is called an "ALD-window". Initially it was used to describe the temperature range where the growth rate was constant, however, it is also being used for the temperature range where self-limiting growth is obtained. Another important aspect of this technique is the ability to mix binary processes to get complex stoichiometry. The good control of each layer deposited enables good stoichiometric control. This will be elaborated further in chapter 2.4.1. Shortcomings of this process are a slow growth rate (thickness deposited per ALD cycle) and in some cases that it covers all available surfaces. Most ALD reactors operate under vacuum. In order to increase deposition throughput and simplification of the process, industries utilizing ALD use big batch reactors[28]. There are also processes that operate under atmospheric pressure such as spatial atmospheric ALD[29].

ALD was initially invented to enable production of large thin film electro luminescent (TFEL) displays. The need for uniform, pin-hole free films on large surfaces was enabled by the use of ALD[30-32]. Since its discovery, the technique has gained a lot of interest, and the number of applications using this method is increasing. It is a good tool for research in the laboratory, due to the good control of the growth, but it is also a vital technique for some industries, and the development of batch processes and atmospheric pressure

processes makes it more available for use on the large industrial scale. There is a plethora of application areas where the ALD technique can be utilized such as; protective coatings (chemical, mechanical, electrical), front contacts, solar cells, decorative coatings, deposition on complex surfaces, lithium battery materials, hybrid material, bio-compatible materials, transistors and within display-technology[25].

The process described above is sometimes referred to as normal or thermal ALD. Plasma Enhanced ALD (PEALD) and spatial atmospheric ALD (AALD) will not be described here, and note that the technique might also be mentioned under other names[25, 26].

2.4.1 The surface utilization concept

The ALD growth mechanism is based on self-limiting surface reactions. When the precursor molecule is adsorbed, it will occupy space on the surface. The size of the precursor is dependent on the type of ligands used, i.e. a precursor consisting of a metal ion and large organic ligands will occupy more space than a metal halide precursor. The size that is occupied by the precursor can be called the surface utilization. The growth rate of a binary compound, such as the process using TMA and water to deposit aluminum oxide, is dependent on its surface utilization. The aluminum oxide process using TMA has a high growth rate due to the small precursor molecules. Calculating the size an adsorbed precursor molecule occupies on the surface is cumbersome, luckily Ylilamm has shown that for many ALD processes the growth rate is inversely proportional with the size a precursor molecule occupies on the surface[33]. If two or more binary processes are combined together, the processes might influence each other. Nilsen *et al.* proposed the surface utilization concept[34] where experimental data can be fitted to a model to describe the growth when several processes are combined. In this concept the growth rate of the individual processes are modified to fit the experimental data.

Let us look at the case of mixing copper oxide and aluminum oxide as an example to describe the concept. Their individual growth rates are v_{Cu} = 0.038 nm/cycle and v_{Al} = 0.115 nm/cycle respectively. Relative growth rates are used in this concept and the growth rate of aluminum oxide is said to be 1. The relative growth rates are given by equation 2.4 and 2.5:

$$u_{Al} = \frac{v_{Al}}{v_{Al}} = 1 \tag{2.4}$$

$$u_{Cu} = \frac{v_{Cu}}{v_{Al}} = 0.33 \tag{2.5}$$

Where $u_{Al/Cu}$ are the relative growth rates for the oxides. Based on this the mol%, or here *cat%,* of copper and aluminium can be calculated from equation 2.6 and 2.7:

$$cat\%_{Cu} = \frac{sub\ cycles\%_{Cu} \cdot u_{Cu}}{sub\ cycles\%_{Cu} \cdot u_{Cu} + (1 - sub\ cycles\%_{Cu}) \cdot u_{Al}} \tag{2.6}$$

$$cat\%_{Al} = 1 - cat\%_{Cu} \tag{2.7}$$

Where $sub\ cycles\%_{Cu}$ refers to the amount of Cu-O cycles with respect to all cycles of binary processes (Cu-O cycles + Al-O cycles). Equation 2.6 can be plotted together with the experimentally obtained values for $cat\%_{Cu}$. The model can be fitted to the experimental data by varying the relative growth rate for CuO, u_{Cu}. The deviation between the fitted model and the initial model can then give indications to how the growth of the binary oxides is influenced when they are mixed together. Fig. 20 and Fig. 21 show how the model can be fitted to experimentally obtained data. The deviation between the initial and fitted model give indications to how the processes influence each other. It is generally expected that the growth rate for a multicomponent complex oxide will be lower than expected from individual growth rates of the binary components[35, 36],However, this is not the case for the Cu-Al-O and Cu-Y-O systems as seen in Fig. 22. A similar behavior has previously been seen for deposition of $PbTiO_3$[37] and Y:ZrO_2 [38].

2.5 Materials

Conventional n-type TCO materials are mainly based on CdO, In_2O_3, SnO_2, ZnO or Ga_2O_3 and mixed compositions of these binary oxides[19]. The combination of optical transparency and electronic conductivity was first discovered for CdO in 1907[39], but has not been commercially used. SnO_2, and its doped versions, has been used in special heating applications since the 1970's and is still a good candidate for several applications such as low emission-windows[24]. As mentioned in chapter 2.3 ITO is the most widely used TCO

today. Presently, no good p-type TCO material exists, and the search for such a material is still a hot topic, especially since conversion of present n-type TCO materials into p-type by heavy doping has not been successful[20].

The current chapter is devoted to the materials studied in this work.

2.5.1 ZnO

ZnO is the material that most probably will replace ITO[40] as TCO material according to the current progress. ZnO is a non-toxic, abundant wide band-gap semiconductor. The optoelectronic properties of ZnO fulfill the requirements mentioned in Section 2.2.1. It has a band gap of 3.37 eV, transparency > 80% and resistivity of $2 \cdot 10^{-4}$ Ω cm[41]. The thin films are produced using conventional, industrial processes at temperatures below 200 ºC[12]. ZnO is natively n-type, (also called intrinsic n-type). To achieve a resistivity near $2 \cdot 10^{-4}$ Ω cm, however, the material needs to be doped. Common dopants are Al and Ga[41], but Ti, B, In and others are also being studied[12]. To fully understand and optimize the material, both the effects of native dopants and intended and unintended dopants needs to be understood. The origin of the native n-type conductivity in ZnO is still a debated subject. Previously, oxygen vacancies were thought to be the main contributor to the n-type conductivity in ZnO, but recent studies have shown that the oxygen vacancies act as deep-level donors. It is more likely that hydrogen contributes to the n-type conductivity by forming defect complexes with the native defects such as oxygen vacancies or with impurity defects and deliberate dopants[42]. Hydrogen is present under almost all growth processes and will therefore contribute to the conductivity of the resulting ZnO material[19].

ZnO crystallizes in the hexagonal wurtzite structure. Most of the deposited ZnO thin films are polycrystalline where preferred orientation often is observed. Thin films of ZnO have been deposited with most of the applicable thin film techniques. The most commonly used are sputtering[43], molecular beam epitaxy (MBE)[44], pulsed laser deposition (PLD)[44, 45], metal organic chemical vapor deposition (MOCVD)[46] and the number of publications reporting use of ALD to deposit thin films of ZnO is rapidly increasing[47]. A good overview of the work done by ALD can be found in the review articles by Miikkulainen et al[25] and Tynell et. al.[47].

Several precursors have been tested for deposition of ZnO using ALD[25, 47]. The most commonly used precursor is diethyl zinc (DEZ)[47]. Normally, the ALD-window (constant growth) is reported to be between 110 – 170 ºC with a growth rate 0.18 nm/cycle – 0.2 nm/cycle. However, uniform films can be deposited at lower and higher temperatures, but the growth rates seem to vary a lot between reports[47]. Other oxygen sources apart from water are also being used[47]. Films deposited using DEZ and water show a good crystallinity even at low temperatures. The films show preferred orientation that seem to vary with deposition temperature. The resistivity of ZnO films deposited using DEZ and water seem to decrease with increasing deposition temperature. The lowest resistivity is achieved at temperatures around 200 – 220 ºC and is as low as 10^{-3} Ω cm[47]. With additional intentional doping the conductivity can be increased further. A typical dopant for ZnO is Al (AZO). Using techniques such as PLD and sputtering has resulted in films with resistivity lower than 10^{-4} Ω cm[48] while for films deposited using ALD it is normally an order of magnitude higher.

2.5.2 SnO_2

Tin(IV) oxide (SnO_2) is an important and widely used wide band gap semiconductor. It is of great interest in corrosive environment applications due to its high stability. This includes applications such as gas sensors[49], batteries[50, 51], infra-red reflection layer on windows for energy conservation (low e-windows) [52] and in photovoltaic applications[52-54].

SnO_2 occurs in nature as the mineral Cassiterite, which possesses the rutile crystal structure. SnO_2 is a native, n-type semiconductor with a wide band gap of 3.6 eV. The lowest resistivity obtained for doped SnO_2 is in the order of 10^{-4} Ω cm for Sb- or F-doped SnO_2 deposited using pulsed laser deposition (PLD) and sputtering[55]. Resistivity of the same order of magnitude has also been achieved using chemical vapor deposition (CVD), but only at temperatures above 300 ºC[56], which is too high for most of the applications. The origin of the n-type conductivity in SnO_2 is believed to be caused by oxygen vacancies[57] and as in ZnO, interstitial H can create shallow donor levels in the band gap of SnO_2[42]. Being such an important material, its properties has been extensively studied and reported previously in review papers such as Refs. [12, 19, 58] .

Thin films of tin oxide has previously been deposited by numerous different types of techniques including wet chemical processes, physical deposition techniques i.e., sputtering and gas phase deposition techniques like chemical vapor deposition (CVD) and also atomic layer deposition (ALD)[19, 58]. Table 1 show the numerous processes reported used with ALD.

Table 1 ALD processes for deposition of SnO_2 published before June 2014. Literature published before December 2010 is taken from the review by Miikkulainen et. al.[25]. Note that temperature window vary between reports and substrates used.

Sn-precursor	**Oxygen source**	**ALD-window (temperatures tested) (ºC)**	**Reference**
Sn	O_2	300	31
$SnCl_4$ - Sb-doped - ITO	H_2O	150- 500 (150-600) 500	52, 59-80 52 81
$SnCl_4$	H_2O_2	250-500 (150-700)	49, 70, 82-86
SnI_4	O_2	500-750 (350-750)	49, 70, 82, 87-90
SnI_4	H_2O_2	600	70
$Sn(CH_3)_4$	N_2O_4	400-450 (375-475)	91, 92
$Sn(CH_2CH_3)_4$ - F-doped	N_2O_4	250-290 (225-325)	91
Dibutyltindiacetate $(CH_3CH_2CH_2CH_2)_2Sn(OCOCH_3)_2$	O_2^P	300-400 (200-400)	51, 93-100.
Tetrakis(dimethylamino) tin, TDMSn, $Sn(N(CH_3)_2)_4$ - ITO - Nb-doped	H_2O_2	50-325 (50 -400) 275	.53, 54, 101 53 102
$Sn(NMe_2)_4$ - ZTO	H_2O	30-200 (30-200) 120 -150	103-105 105-107
Sn(tbba) tbba=N^2,N^3-di-tert-butyl-butane-2,3-diamidotin(II) - $(Sn,Al)O_x$ - ZTO	H_2O_2	50-150 (50-250) 120 170	.108 109 110
Sn(tbba)	NO	130-250 (130-280)	111
$Sn(OC(CH_3)_3)_4$	CH_3COOH	(75-250)	112, 113
$Sn(dmamp)_2$ [dmamp = $OC(CH_3)_2CH_2N(CH_3)_2$	O_2^P	50-200 (50-200)	114
Tin(IV)-butoxide	O_2^P	200	50
$Sn(acac)_2$ (acac=acetylacetonate)	O_3	175-300 (100-375)	115

P=plasma enhanced ALD (PEALD)

The first report of SnO_2 films deposited by ALD was with elemental tin as the metal precursors. Later, tin halogens such as $SnCl_4$ and SnI_4 have been reported as suitable tin precursor. They have been used together with oxygen precursors such as H_2O, H_2O_2 and O_2. A few attempts using organometallic compounds have been reported, while in recent years more focus has been on metal organic precursors both using plasma enhanced ALD (PEALD) and thermal/normal ALD. However $SnCl_4$ and H_2O is still the precursor pair most reports published have used. A few attempts to dope SnO_2 or to make ternary oxides have also been reported as listed in Table 1. The main focus for articles published the last couple of years focus on deposition of SnO_2 on nanostructures such as nanowires, nanotubes and high aspect ratio substrates[51, 99, 112].

2.5.3 Delafossite - $CuMO_2$

In this work, one of the goals has been to synthesize thin films with the delafossite type structure. Many of the interesting properties for this class of oxides stem from copper oxide, so before describing the delafossites some notes on copper oxides and previous work done by ALD will be presented.

Copper oxide

Copper oxides are applicable within numerous areas e.g. catalysis [116], high temperature superconductors [117], gas sensors[118] and photovoltaics [119, 120], among others. In binary compounds, copper takes oxidation states +I and +II in Cu_2O and CuO, respectively [121], whereas +III and mixed valence +II/+III occur in ternary and other complex oxides. Both of the binary copper oxides are p-type semiconductors and Cu_2O has long been regarded as a good candidate as a low-cost, non-toxic absorber material for application in solar cells[120, 122-126].

Cupric oxide (CuO) has been a hot topic among the studies on transition metal oxides because of its interesting properties as a p-type semiconductor with a narrow band gap (1.2 eV in bulk) and as the basis of several high-temperature superconductors and giant magneto resistance materials[127]. Cuprous oxide (Cu_2O) is one of the first known p-type semiconducting materials[125, 126, 128]. Cu_2O and CuO have striking contrasting colors, crystal structures, and physical properties[127, 129]. Cu_2O is a reddish p-type semiconductor of both ionic and covalent nature with cubic structure (space group $Pn\overline{3}m$). By contrast, CuO has

an iron-dark color with a more complex monoclinic tenorite crystallographic structure (space group, C2/c). The crystal structures of the two binary oxides are shown in Fig 8. Cu_2O is expected to have an essentially full Cu 3d shell with a direct forbidden band gap of 2.17 eV in bulk. CuO has an open 3d shell with a direct band gap (1.2 eV in bulk) of charge-transfer type [127]. Recent reports have demonstrated that CuO has higher conductivity than Cu_2O but with lower carrier mobility [127].

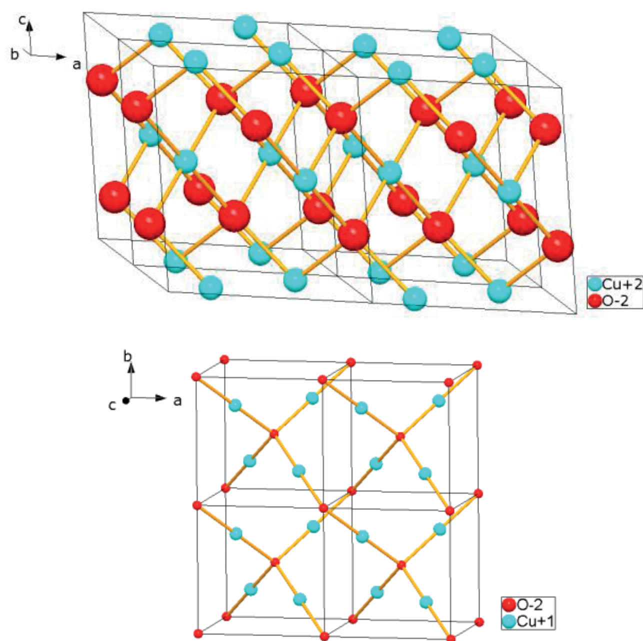

Fig 9 crystal structure copper oxides (top) **cupric oxide, CuO and (bottom) cuprous oxide, Cu_2O.**

Copper oxides have previously been deposited by ALD. Much of the work reported has had the main purpose to reduce deposited copper oxide in order to produce films of metallic copper, both by *in-situ*[130] and post[131] deposition reduction. Several precursors have been tested. $Cu(thd)_2$ (thd=2,2,6,6-tetramethyl-3,5-heptanedionato) and air [116, 132-134] for preparation of catalysts. $Cu(hfac)_2$ (hfac=hexafluoroacetoacetonato) and H_2O [130], CuCl and H_2O [130, 135], CuCl and H_2O/O_2 [136], Bis(tri-n-butylphosphane)copper(I)acetate and H_2O/O_2 [131, 137, 138]. Utrianinen *et al.* in Ref. [139] has suggested that a reaction between $Cu(acac)_2$ (acac=acetylacetonate) and water can be suitable for formation of thin films of copper oxide that subsequently can be reduced to metallic copper. van Welzenis *et al.* used in Ref. [140] the reaction between $Cu(acac)_2$ and O_2/air to demonstrate ALD growth by

performing *in-situ* low energy ion scattering (LEIS). The objective of this set-up was to investigate sub-monolayers of metals on oxide substrates, and the deposited copper oxide was therefore reduced to metallic copper. Other precursors using PEALD[141] and AALD[142, 143] have also been reported, but will not be presented further here.

The highest deposition temperature for the process using $Cu(thd)_2$ and air is 170 ºC due to decomposition of $Cu(thd)_2$ at 190 °C[132]. The reaction between $Cu(hfac)_2$ and H_2O needs a deposition temperature of 210 º C to take place. At a deposition temperatures of 300 ºC the as-deposited films show signs of decomposition[130]. Using CuCl as a copper precursor requires deposition temperatures above 375 ºC[135, 136]. When H_2O is used as the oxygen source together with CuCl, formation of HCl can lead to etching and non-uniform films[130]. The highest growth rate when using CuCl is 0.14 nm/cycle at optimized conditions. The growth rate is highly dependent on temperature and substrate. For the process using Bis(tri-n-butylphosphane)copper(I)acetate and H_2O/O_2 a narrow temperature window of 100 – 130 ºC is seen with a growth rate of about 0.01 nm/cycle. This process has been reported to be highly dependent on the substrate used[131].

Delafossite - Cu*M*O_2

The current major limiting factor in realization of transparent electronics is still insufficient properties of present p-type TCO's[144, 145]. Current p-type oxides are mainly based on transition metal oxides, e.g. CuO[146], Cu_2O[124], NiO[147], Co_3O_4[148], MnO_2[148], Fe_2O_3[148], amongst others. These materials are limited by their low conductivity, perhaps with the exception of Cu_2O[120, 123, 124], low band gap and/or coloration due to d-d transitions.

Despite a semi-low band gap, Cu_2O is presently a good candidate as p-type TCO material. Cu_2O adopts the cuprite structure which contains linear O-Cu-O fragments, with oxygen tetrahedrally coordinated by copper. The origin of the p-type conductivity stem from copper vacancies in the structure[120]. In 1997 Kawazoe et al. suggested that $CuAlO_2$, taking the delafossite type structure, would be a good candidate as p-type TCO material. The delafossites are generally of the form of $A^IB^{III}O_2$, where A^{I+} represents the monovalent cation (e.g. Cu^+, Ag^+ amongst others) and B^{III+} (e.g. Al^{3+}, Y^{3+}, Fe^{3+}, Cr^{3+}, In^{3+} to mention a few) represents the trivalent cation. The structure, as shown in Fig 10, consists of an alternative stacking of A^I and layers of $B^{III}O_2$ composition, consisting of $B^{III}O_6$ octahedra sharing edges. Each A^I atom is linearly coordinated with two oxygen atoms to form an

O−A^{I}−O dumbbell unit placed parallel to the c-axis. O atoms of O−A^{I}−O dumbbell link all A^{I} layers with the $B^{III}O_2$ layers. Two alternative layer stacking sequences are possible, resulting in a hexagonal (space group $P6_3/mmc$) or rhombohedral (space group $R\bar{3}m$) unit cell[149, 150]. $CuAlO_2$ have the rhombohedral structure. Ternary metal oxides, ABO_2, having this type of crystal structure include, A= Pd, Pt, Cu, Ag and B=Co, Cr, Rh, Al, Fe, Ga, Sc, Y, La etc. [151, 152]

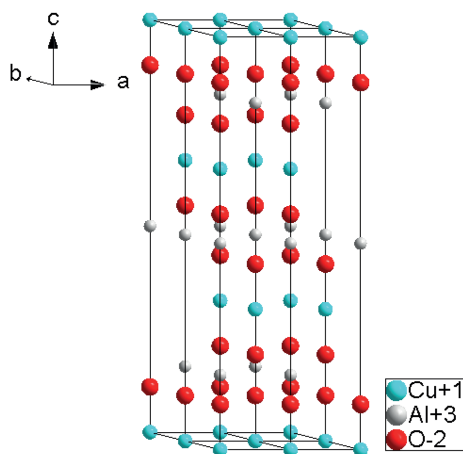

Fig 10 Crystal structure of delafossite, space group $R\bar{3}m$, $CuAlO_2$.

For the Cu^{+} based delafossites, named here as CuMO_2, the p-type conductivity in these materials is thought to stem from copper vacancies and oxygen interstitials [150, 153]. In $CuAlO_2$ both copper vacancies and oxygen interstitials have low formation energies. However, the oxygen interstitials seem to form deep acceptor levels[154]. Doping of delafossite materials can be achieved by replacing the M^{3+} with either a divalent ion to achieve acceptor doping or with a tetravalent atom to obtain donor doping. It has been reported that $CuInO_2$ can be doped both p- and n-type[155-158] using Ca^{2+}[156, 158] and Sn^{4+}[156, 157] as acceptor and donor dopants respectively. Table 2 show examples of some copper based delafossites and their optoelectronic properties.

Table 2: Examples of optoelectronic properties for selected un-doped and doped delafossite thin films. (the table is based on table 12.4 in Ref.[152] with some modifications) All films show p-type conductivity except for Sn-doped $CuInO_2$.

Material	Direct band gap, E_g (eV)	Average Film Thickness (nm)	Transparency (%)	Conductivity ($S\ cm^{-1}$)	Ref.
$CuAlO_2$	3.5	230	70	0.34	159
$CuGaO_2$	3.6	500	80	0.063	160
$CuInO_2$	3.6	500	-	0.052	157
$CuIn_{1-x}Ca_xO_2$ (x=0.07)	~3.9	170	70	0.0028	156
$CuIn_{1-x}Sn_xO_2$ (x=0,05)	~3.9	280	40	0.0038	156
$CuCrO_2$	~3.1	250	40	1	161
$CuCr_{1-x}Mg_xO_2$ (x=0,5)	3.1	270	50	220	161, 162
$CuYO_2$	~3.5	200	60	0.025	162, 163
$CuY_{1-x}Ca_xO_2$ (x=0.1-0.2)	3.5	240	50	1.05	162, 163

This class of material have been suggested for several possible applications such as: hydrogen production in photocatalysis[164, 165], oxygen storage for use in catalyst for exhaust gas[166], catalyst in hydrogenolysis[167], spin-driven multiferroicity[168], ozone sensor[169], as well as candidate for use in photovoltaics[170, 171].

The delafossites are only formed by annealing above 1000 ºC[172, 173]. Fig. 11 show phase diagram for CuO-Al_2O_3, Cu_2O-Al_2O_3 and CuO-Y_2O_3. $CuAlO_2$ is readily formed by annealing above 1000 ºC[173]. However, to obtain $CuYO_2$ the sample first needs to be annealed above 1000 ºC to form $Cu_2Y_2O_5$. The $Cu_2Y_2O_5$ will then have to be annealed above 1100 ºC under controlled oxygen partial pressure to obtain the delafossite type phase. [170, 172]. Several thin film techniques have previously been used for deposition of delafossites, such as: laser ablation[171], pulsed laser deposition (PLD)[156, 160], chemical vapor

deposition (CVD)[174], reactive sputtering[175], rf magnetron sputtering[176], sol-gel[177] and dip-coating[178].

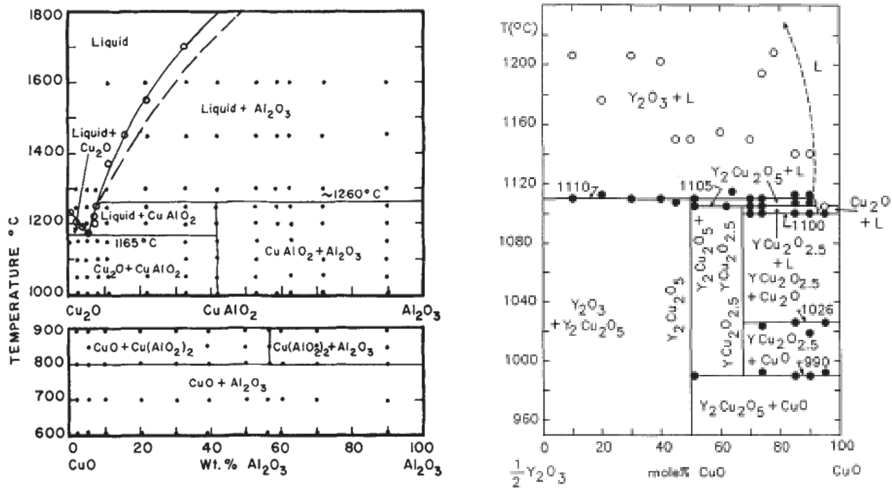

Fig 11 Phase diagram of (left) CuO-Al_2O_3 and Cu_2O-Al_2O_3 adapted from Ref. [173] and (right) Pseudo-binary phase diagram of the Y_2O_3-CuO system in air (the indicated condensed phases are all in equilibrium with air): (•) phase change and (O) partial melting. Adapted from Ref.[179]

3 Characterization methods

The characterization methods used in this work are standard methods within materials research. In this chapter a brief overview of the principles for a selection of these methods will be given. For further information regarding the experimental set-up on the specific studies the reader is advised to look in the experimental sections in the attached papers and manuscripts.

3.1 X-ray based methods

X-ray based methods are some of the most widely used techniques in materials science. X-rays are photons with wavelengths in the order of one tenth of a nanometer. When X-rays interact with a material it can either undergo elastic- or inelastic scattering. The different ways the photons are scattered can give information about the materials properties. The wavelength is similar to the distance between crystal planes in a crystalline material and so the beam can be diffracted, it can also be reflected, polarized and interference can occur. If inelastic scattering occurs, core electrons in an atom can be excited to an outer electron shell. When the electron relaxes it will emit light specific for the atom (X-ray fluorescence). If the electron absorbs more energy, it can be ejected to vacuum (photoelectric effect) and an ion is formed. The penetration depth of X-rays in a material increases with decreasing wavelength. All of these phenomena can be used to find material properties such as identification of crystal structure, composition, binding energies, thickness of thin films, and size of crystallites.

3.1.1 X-ray diffraction (XRD)

When a beam of X-rays hits a crystalline material, the crystal planes will act as a diffraction grid. By knowing the wavelength, λ, of the incoming X-rays and the angle, θ, between the incoming beam and crystal plane, the distance between the crystal planes, d, can be determined using Bragg's law shown in Eq. 3.1[180].

$$n\lambda = 2d_{hkl}sin\theta \qquad (3.1)$$

Where n is an integer 1, 2, 3…, typically 1. The intensity of the diffraction peaks are influenced by the crystal symmetry and the type of atoms the crystal is built up from.

X-ray diffraction analysis can be carried out using different X-ray sources and configurations for the angle of the incoming and outgoing beam. Normally these are synchronized, equal, related to the sample surface. This type of geometry is called Bragg-Brentano geometry. In this type of geometry only the crystal planes parallel to the sample surface will be detected. In typical powder diffraction system a diverging monochromatic beam is used. The diffracted beam will converge and focus on the diffraction circle. For thin film tools there is often a Göbel mirror that can convert the divergent beam into a parallel beam. This is important when analyzing at low angles such as for X-ray reflectometry (see chapter 3.1.2).

In Bragg-Brentano geometry the penetration depth of the beam can be several micrometers into the sample, when analyzing thin films it can in some cases be advantageous to use Gracing incidence configuration (GIXRD). Here the incident beam is sent into the sample at a small angle so that it graces the surface. The detector can then be moved along the diffraction circle. In this configuration the incident beam should have an angle slightly above the critical angle of the material.

For laboratory diffractometers the X-ray sources are normally monochromatic and based on $K_{\alpha 1}$ radiation. In this case a Cu source was used with a wavelength, λ =1.54060 Å. Some selected samples were also analyzed using a synchrotron source, then called synchrotron X-ray diffraction (SXRD). When particles such as electrons are accelerated to great speed in a magnetic field they emit electromagnetic radiation. This is the principle for a synchrotron light source. The radiation obtained has a wide range of wavelengths enabling optimal experimental conditions and the high intensity ensures faster data collection.

3.1.2 X-ray reflectometry (XRR)

XRR is widely used to characterize thin films and multilayer structures. The technique can give information about the density of the material, film-/layer thickness and surface- and interface roughness. The technique is based on specular reflectivity (reflected angle equal

to incident angle)[181]. When the X-ray beam is sent towards the sample at very low angles (0 – 0.5º) it will be totally reflected before it reaches the critical angle. The critical angle varies depending on the density of the material. For angles above the critical angle the X-rays will penetrate the sample, and be reflected by all transitions in X-ray density. This can then result in interference. Based on Parratt's formalism the interference pattern (Kiessing fringes) obtained can be used to find the thickness of the layer. Surface roughness reduces the intensity of the specular reflected beam. By fitting the data to calculated models these three parameters can be found. The total scan range is usually less than 0 - 5°.

3.1.3 X-ray fluorescence (XRF)

XRF is a quantitative method to analyze the chemical composition in a sample[180]. When used to analyze thin film samples the technique requires a calibration procedure[182]. If correctly calibrated it can give the relative amounts of the specific elements in the sample. XRF is based on inelastic scattering between X-rays and core electrons in an atom. The electrons can then be excited to an outer electronic shell. When the electron relaxes it will emit light specific for the energy levels in the atom. X-rays with wavelengths from 0.01 – 2.0 nm is used. The peaks obtained in the spectra identify atoms present while the intensity gives information regarding the amount of the atoms in the sample. The instrument used in this work can detect concentrations from ppm to 100%, but in practice the level is closer to 1% for analysis of thin films. In theory, the XRF has the ability to detect X-ray emission from virtually all elements, depending on the wavelength and intensity of the incident X-rays. However, in practice, most commercially available instruments are very limited in their ability to precisely and accurately measure the abundances of elements with an atom number lower than 11. XRF analysis cannot distinguish ions of the same element in different valence states.

3.1.4 X-ray photoelectron spectroscopy (XPS)

XPS is used to analyze composition and oxidation state in a material[180]. XPS is based on inelastic scattering of X-rays. Electrons are then ejected from the material (photoelectric effect). In this technique X-rays with longer wavelengths are used. This enables a surface sensitive technique since the penetration depths of the X-rays is low. To achieve a depth profile in a sample sputtering is often used. In this technique the energy of the ejected

electron is measured, by knowing the work function of the material and the energy of the incoming X-ray photon. The binding energy of the electron that has been ejected can then be found. The binding energy is specific and can therefore be used to identify the atom and the oxidation state. In this work a standard was used to help with the interpretation of the data.

3.2 Optical spectroscopy

The importance of knowing how a material interacts with light in the ultra violet (UV) – visible (vis) – infra red (IR) range has already been mentioned earlier in chapter 2.2 and 2.3. In order to determine whether a material is transparent optical measurements are a necessity.

3.2.1 Spectroscopic Ellipsometry (SE)

SE is an optical analysis technique for investigating the thickness and the refractive index of thin films. SE measures the difference in reflectivity of s- and p-polarized light. The measured data needs to be fitted to theoretical models to find the desired properties. This technique is dependent on samples that do not absorb all the incoming light. Materials that absorb in the wavelengths measured by the instrument require more complex models to fit the data.

3.2.2 UV-VIS-NIR spectroscopy

As described earlier, light that is shone on to a material can either be reflected, transmitted or absorbed. The way a material interacts with light with varying wavelengths can give useful information about the material in question. Here the UV-vis-IR light is used. By doing UV-VIS-NIR spectroscopy on TCO materials it is possible to determine the optical band gap of the material using Tauc plots[183] for the absorption around the fundamental absorption edge in the UV region. Absorption in the visible range can indicate impurities while the absorption/reflection in the near infra-red region gives an indication on the carrier concentration. This is also an important feature if the material is to be used as front contact on a solar cell that utilizes the NIR radiation.

3.3 Electrical Characterization

When analysing a TCO material the electrical properties are as important as the optical. Simple resistivity measurements will easily determine whether the material is a suitable candidate as an electrode, while more complex measurements can give further understanding of the behavior of the material.

3.3.1 Four-point-probe Measurements

Four point probe measurements are used to characterize the resistivity of a bulk or thin film sample. By utilizing a four probe set-up the resistivity measured belongs to the film only and not being affected by the contact point which would have been the case for a set-up with just two electrodes. Fig. 12 shows the set-up for a four point probe measurement. A current, I, is sent through the sample and the voltage, V, is measured as shown in Fig. 12. The specific resistivity for the sample can then be calculated.

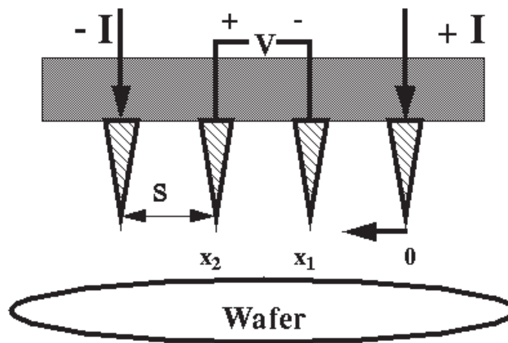

Fig 12 Schematic of 4-point probe configuration, Picture adapted from Ref[184].

For the calculations some assumptions have to be made. The metal tip is infinitesimal and samples are semi-infinite in the lateral dimension. For bulk samples where the sample thickness t >> s, the probe spacing, it is assumed that a spherical protrusion of current emanate from the outer probe tips. The differential resistance (R) is given by equation 3.2:

$$\Delta R = \rho \frac{dx}{A} \tag{3.2}$$

where ρ is the specific resistivity. A indicates a general area. In the case of a thin film where t is much smaller than s, the current through the sample can be described as rings. The area can be described as equation (3.3):

$$A = 2\pi xt \tag{3.3}$$

The resistivity in the sample is then calculated from equation (3.2), which gives equation (3.4):

$$R = \int_{x_1}^{x_2} \rho \frac{dx}{2\pi xt} = \int_{s}^{2s} \frac{\rho}{2\pi t} \frac{dx}{x} = \left[\frac{\rho}{2t\pi} \ln(x) \right]_s^{2s} = \frac{\rho}{2t\pi} \ln 2 \tag{3.4}$$

By using Ohm's law, $R=V/I$, expression 3.4 can be generalized to equation 3.5 giving the specific resistivity of the film.

$$\rho = \frac{t\pi}{\ln 2} \left(\frac{V}{I} \right) = \frac{t\pi}{\ln 2} R \tag{3.5}$$

3.3.2 Van der Pauw and Hall measurements

The conductivity in a semiconducting material is influenced by the mobility of the charge carriers and the carrier concentration (see equation 2.1). In the van der Pauw method the sheet resistance of the film is found, from this one can obtain the specific resistivity. By applying a magnetic field and measure the voltage that is built up (called Hall-voltage[183]) one can find the carrier concentration, if the thickness of the film is known. The method will also indicate whether the carrier concentration is dominated by holes or electrons. By measuring the specific resistivity and carrier concentration the mobility can be calculated using equation 2.1. (Note: $\sigma=1/\rho$)

3.4 Secondary Ion Mass Spectroscopy (SIMS)

SIMS is a quantitative method to analyze concentrations, identify impurities and obtain depth profiles of atoms in a sample[180]. The instrument used in this work has a detection limit of 10^{13} – 10^{16} atoms/cm^3 and depth resolution of 2.0 nm. In this method an ionic beam is rastered over the sample surface. The ion beam could be O_2^+ or Cs^+. The type of beam selected is based on whether one wants to detect negative or positive ions. When the ions in the primary beam hit the material the surface is sputtered. This results in a second beam that is analyzed using for instance a magnetic sector as has been used in this work. To obtain doping concentrations standards are used to calibrate the instrument.

3.5 Atomic Force Microscopy (AFM)

As the name of the technique implies, it provides a surface topography by scanning the force (van der Waals) between a tip integrated on a cantilever and a surface. The tip is often made of silicon or silicon nitride with a width of ~10 nm. There are three main modes for AFM aquisition; contact mode, tapping or intermittance mode, and non-contact mode. Tapping mode has been used for most of the results acquired in this work. In tapping mode, the cantilever is set in resonant vibration, which is affected by the van-der-vaals forces between the tip and the surface as it approaches the sample surface. A topography image is acquired by scanning the tip over the surface while monitoring the resonant frequency. The technique is very suitable for obtaining direct information on topography effects such as surface roughness and crystallite features, however, one must bear in mind that the topography image is convoluted by the shape of the tip used[185].

4 Present work – results and discussion

This work has focused on three materials, namely ZnO, SnO_2 and $CuAlO_2$. The ZnO and SnO_2 are well known n-type TCO materials and ALD processes for these materials have been reported by several other groups (see chapter 2.4.1 and 2.4.2). Our contribution has been to look into already known processes or study a new process to better understand the process and the resulting film material. The last material, $CuAlO_2$, has not been deposited using ALD before. As part of the study to deposit the $CuAlO_2$ a new process to deposit CuO has been studied. Depositions containing Cu-Y-O was done together with the Cu-Al-O system in order to investigate the flexibility of this deposition system.

4.1 ZnO

Deposition of ZnO using ALD has been a small part of this work. Most of the work has been in collaboration with others. In this part some unpublished results related to analysis of impurities in the as-deposited films will be presented. The candidate has contributed with samples and XRD characterization for two papers, Refs.[186, 187], which will be summarized below.

4.1.1 Diethyl zinc (DEZ)

ALD is referred to as a self-limiting process. The metal precursors are liquids or solid compounds and can be heated to reach a sufficient vapor pressure. If there are impurities in the precursor with a higher sublimation temperature they will not be transported to the reaction chamber in any significant amount. If the impurities have a sublimation temperature lower or similar to the precursor, the amount of transported impurity will be significant until the volume of impurities in the starting material diminishes. Al-doping is typically used to obtain highly conducting ZnO films. The reaction between DEZ and H_2O is the most commonly used process in ALD to deposit ZnO and is the process that has been used in this work. It was therefore interesting to see whether the Al content in the as-

deposited films using two different diethyl sources varied. Two different DEZ precursors were tested to see if the Al content in the films varied. Diethyl zinc from EMF Speciality Chemicals and diethyl zinc for Cambrige Nanotechnology Inc. for ALD systems from Aldrich were tested. EMF informs that their product is Epipure and that the level of impurities is below 1 ppm. They claim that the main impurities are Sn, Si and Al. Aldrich informed that they have tested the purity with respect to the Zn content. And inform that the purity with respect to the metal content is 99.4%. They do not have any information related to what the impurities are. Based on this films deposited at 175 ºC were analyzed using SIMS, revealing that the major impurities are Al and Si. Since Al is supposed to be a good dopant quantitative analysis was performed. The Al content in the films varied between 10^{18} – 10^{19} atoms/cm^3 for films deposited using the precursor from Aldrich to 10^{15} atoms/cm^3 for the precursor from EMF. However, it is important to note that the amount of Al in the films deposited using the precursor from Aldrich varied with one order of magnitude for different films using the same deposition parameters. Later studies has shown that the amount of Al in the films vary with respect to how much of the precursor has been used[188]. The precursor from EMF was used for the rest of the studies regarding deposition of ZnO.

4.1.2 Heterojunction between ZnO and Si(100) and work function of ZnO

ZnO is a potential candidate as a transparent electrode for optoelectronic devices. It can also form rectifying junctions with other semiconductors such as Si. Heterojunctions between ZnO and Si is of interest for photovoltaic applications. The performance of such a heterojunction is influenced by defects at the interface and formation of SiO_x layer between the Si substrate and ZnO film. The electronic properties for ZnO/Si heterojunctions where the ZnO was deposited using ALD were studied. The films where deposited at 175 ºC using 1375 cycles and a growth rate of ~0.2 nm/cycle. The films were deposited on both n- and p-type Si(100). After deposition the films were annealed for 30 minutes in air at varying temperatures from 200 ºC - 500 ºC. Fig. 13 shows the XRD data for the as-deposited and annealed ZnO samples.

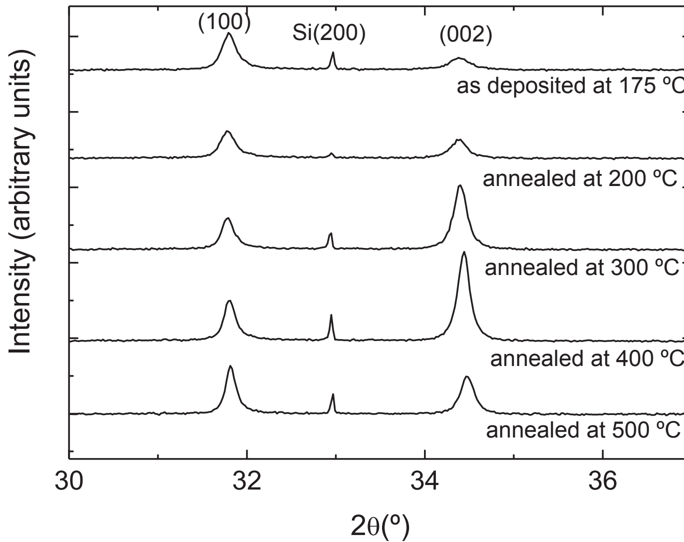

Fig 13 XRD spectra of as-deposited and annealed ZnO films on Si(100).

In Fig. 13 one can observe two peaks corresponding to the (100) and (002) reflections of ZnO in the Wurtzite structure. The lack of the (101) reflection at 2θ = 35.3 º indicates that the ZnO layer is not randomly oriented, but has preferred orientation, in accordance with previous studies[189]. The peak at 2θ = 32.9 º, corresponds to the (200) reflection of Si, it is visible here due to the high amount of silicon as compared to the ZnO film. The as-deposited films show a more intense (100) peak compared to (002). However, by annealing the films, the ratio between the (100) and (002) peaks decreases, and at 300 and 400 ºC, the (002) peak is stronger than the (100) peak. This indicates a change in the preferred orientation from (100) to (002) along the c-axis. In addition, the full width at half maximum (FWHM) becomes narrower with heat treatment. There could be several causes for a change in FWHM; it can be influenced by stress in the film and by the size of the grain in the out of plane direction. A narrowing in the FWHM can indicate a larger grain size. Hence, the heat treatment up to 400 ºC could result in an improvement of the crystallinity along the c-axis, as indicated by the increase of the peak intensity and the smaller FWHM. However, heat treatment at 500 ºC results in a reduction of the (002) peak, which could indicate a degradation of the crystal orientation along the c-axis.

The electrical properties of the interface between the ZnO film and the Si substrate were investigated by deep level transient spectroscopy (DLTS), I-V and CV measurements to investigate the rectification properties of the junction. It was seen that for as deposited films electron traps, defects, exist at the interface. By annealing at 400 ºC one of the defects were removed and the rectification was improved. At higher annealing temperatures new defects were formed at the interface. Investigations using transmission electron microscopy (TEM) showed that a thin layer of SiO_x separated the film and the Si substrate. The work function of the ZnO film was found to be 4.65 eV.

4.2 SnO_2

Even though there are several reports on deposition of SnO_2 by ALD, many of the processes face some challenges. Processes using halogenated precursors might need high deposition temperatures. If hydrogenated oxygen precursors are used, etching of the films might occur during deposition. The resulting films might also contain halides. Incorporation of halides and hydrogen if hydrogenated oxygen precursors are used can on the other hand contribute to better electrical properties in the resulting film. The use of precursors containing organic ligands can lead to contamination of carbon and nitrogen in the films, but these processes often take place at lower deposition temperatures. Taking all of these aspects into account we wanted to study deposition of SnO_2 using SnI_4 and O_3 as precursor at temperatures below 300 ºC. Deposition at high temperature using this precursor combination has previously been presented by A. Tarre et. al. [190].

Another important aspect for having a good SnO_2 process is that due to the materials robustness and chemical stability it can be used as a buffer layer between film and substrate during high temperature annealing, such as we applied for annealing of the Cu-Al-O films in paper III.

4.2.1 ALD process

The operational parameters for the process were determined. It was found that the growth follow the self-limited and linear growth expected by ALD. The process was tested from a temperature of 110 ºC where ALD growth was obtained. Fig. 14 shows the growth rate as

a function of deposition temperature, including the results from A. Tarre et. al. Ref. [190]. The x-ray diffractograms for the as-deposited films are shown in Fig. 15.

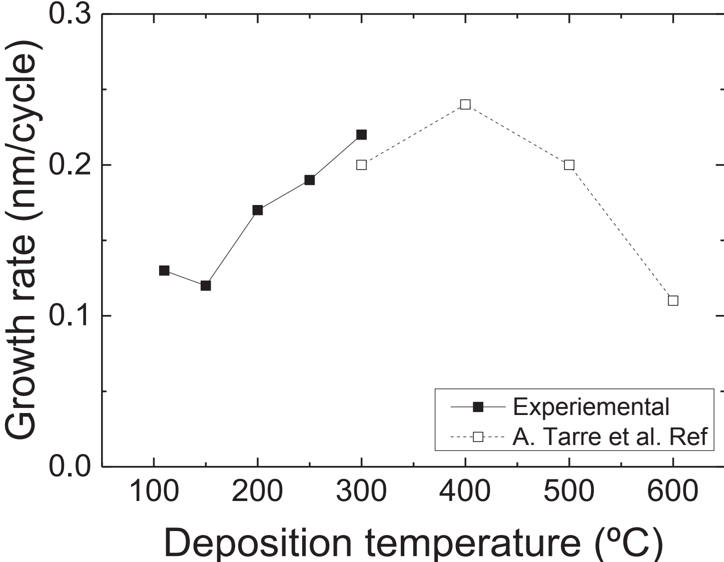

Fig 14 Growth rate as a function of deposition temperature for films grown on Si(111), based on 250 cycles. Open squares are results taken from Aivar Tarre's work in Ref [190].

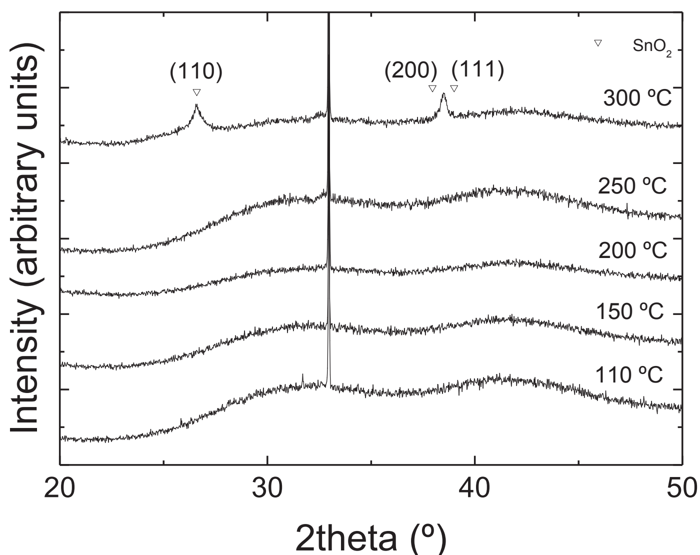

Fig 15 X-ray Diffractogram of as-deposited SnO_2 films on Si(100) substrates at different deposition temperatures indicated on the figure. SnO_2 was identified using the PDF file 00-041-1445. Crystal planes are indicated in the figure.

Based on XRD data in Fig. 15 it seems that all films are amorphous except for the film deposited at 300 ºC. GIXRD measurements were also carried out for the sample deposited at 250 and 300 ºC. No peaks were observed for the sample deposited at 250 ºC. The surface roughness of the samples, as measured by AFM, increased with increasing deposition temperature from 0.25 nm at 110 °C to 0.9 nm at 300 °C. All films were deposited using 250 cycles.

XRF analysis of the as-deposited films was carried out to see whether iodine was incorporated into the film during the deposition. Iodine was detected, but due to the small amount of sample, the uncertainty was too high to give any quantitative number. The detection limit for the XRF instrument used is 1 ppm, resulting in an iodine content below 0.4 at%.

4.2.2 Electrical and optical properties of the as-deposited SnO_2 films

Based on the XRD data it was important to identify how the crystallinity of the films affects the optical and electrical properties of the films. The absorbance spectra, Fig. 16, show that the films are almost identical even though they are deposited at different temperatures and regardless of whether they are crystalline or not. The absorbance (A) was obtained by measuring the transmittance (T) and the specular and diffuse reflectance (R) of the samples. A can then be calculated using equation 4.1:

$$100 = T + R + A \tag{4.1}$$

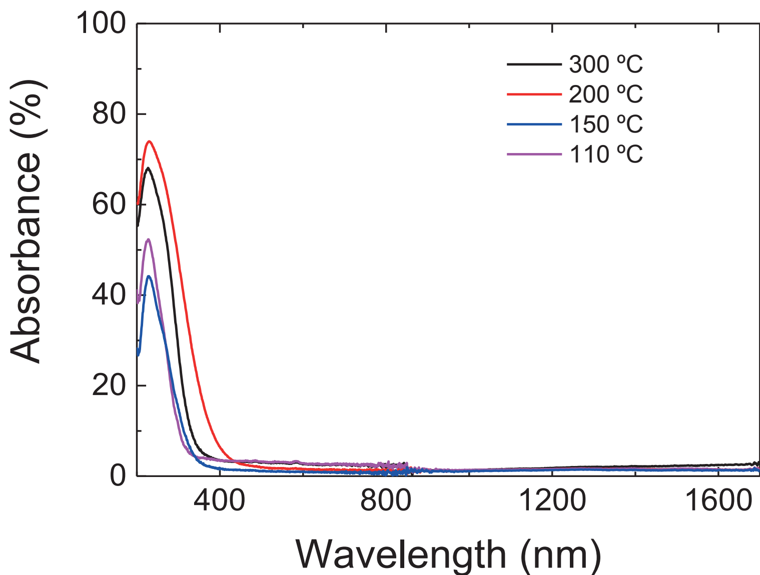

Fig 16 UV-vis-NIR spectra of films deposited at a deposition temperature of 110, ºC 150 ºC, 200 ºC and 300 ºC using 250 cycles. Absorbance obtained by measuring transmittance and reflectance.

Since reflectance and transmittance was measured, one can create Tauc plots for the data obtained close to the fundamental absorption (peak around 300 nm). The Tauc plots and estimated optical band gaps are shown in Fig. 17.

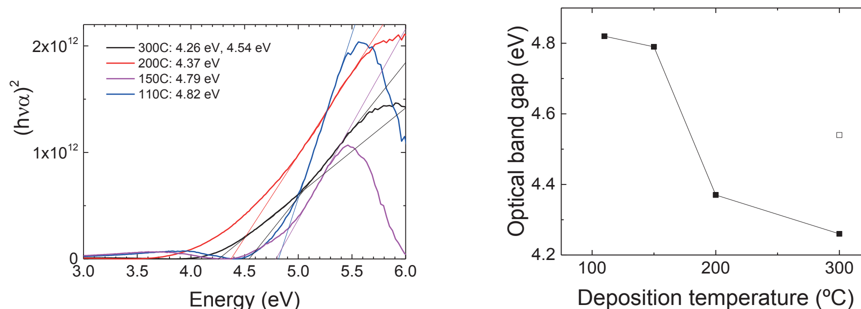

Fig 17 (left) Tauc plots of films deposited at 110, ºC 150 ºC, 200 ºC and 300 ºC using 250 cycles. Linear curve fitting with extrapolation to the x-axis is shown. (right) Optical band gaps are obtained from Tauc plots (left). Open square represents the second linear area seen for the film deposited at 300 ºC.

The Tauc plots indicate that the optical band gap of the SnO_2 films decrease with increasing deposition temperature. However, for the film deposited at 300 ºC it is possible to fit two linear curves to the Tauc plot. The decreasing band gap with increasing deposition temperature has also been reported for other SnO_2 processes using ALD, but they report that the band gap is indirect[103].

The electrical properties of the films were characterized by Hall measurements at room temperature. It was only possible to measure the samples deposited at 200 ºC and above, which had a resistivity of 9 Ω cm, close to the limit of what could be measured. Therefore, the mobility and carrier concentration for this measurement is not included. The resistivity is, however, mentioned to show that for deposition temperatures of 200 ºC and below the resistivity of the films is high. Table 3 shows the values obtained for a sample deposited at 250 and 300 ºC. Both measurements indicated n-type conductivity in the SnO_2 films. The carrier concentration in this process is lower than what has been seen for as-deposited films using $SnCl_4$ and H_2O[52]. One explanation for this could be that no hydrogen is incorporated in the film during deposition. In the process using Sn(tbba) and H_2O/H_2O_2 the carrier concentration is higher than in our films, however, the mobility is lower[108, 110]. It was, however, not expected that the sample deposited at 250 ºC would have similar electrical properties as the film deposited at 300 ºC since it seems to be amorphous based on the XRD data. One explanation for the increased mobility for the sample deposited at 250 ºC could be that the conductivity was dominated by conduction along the grain boundaries,

however, previous experiments have proven the opposite, that the conductivity is typically reduced due to grain boundaries[19, 58].

Table 3: Resistivity, carrier concentration and mobility Obtained from Hall measurements.

Deposition temperature (ºC)	Resistivity (Ω cm)	Mobility (cm^2/Vs)	Carrier concentration (cm^{-3})
250	$7.3 \cdot 10^{-3}$	37	$2 \cdot 10^{19}$
300	$7.1 \cdot 10^{-3}$	17	$5 \cdot 10^{19}$

As a summary, thin films of SnO_2 can be deposited down to a substrate temperature of 110 ºC. However, the electrical properties are strongly dependent on the crystallinity of the films.

4.3 Cu-M-O (M=Al and Y)

$CuAlO_2$ and $CuYO_2$ both have the delafossite type structure and are potential candidates as p-type TCO materials. $CuAlO_2$ was the first material discovered[171] and is widely studied, while $CuYO_2$ has received less attention[153]. A reason for this could be the more complicated synthesis route. In order to study the Cu-*M*-O (*M*=Al or Y) using ALD a new process to deposit CuO was found and combined with known processes for deposition of Al_2O_3 and Y_2O_3. The samples with the correct stoichiometry were annealed to attempt to obtain the delafossite type structure.

4.3.1 Deposition of CuO

A new process for deposition of copper(II) oxide, CuO, was studied in order to obtain better insight into its chemistry. Copper acetylacteonate, $Cu(acac)_2$, was tested with H_2O and with O_3. O_3 was found to react with $Cu(acac)_2$ in an ALD manner providing self-limiting and linear growth. Fig. 18 shows the temperature window for the $Cu(acac)_2$ and O_3 process.

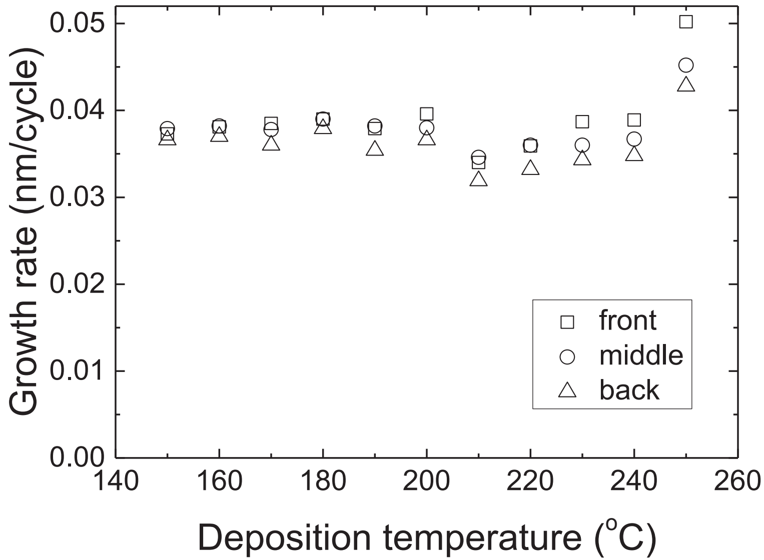

Fig 18 Growth rate as a function of deposition temperature for films grown on Si(111) with a size of 4 x 4 cm^2 using $Cu(acac)_2$ and O_3 for 1000 cycles

Films with a uniform thickness were obtained up to temperatures of 230 ºC. The temperature range from 140 – 230 ºC is in the same range as many other ALD processes such as TMA and H_2O/O_3 to make Al_2O_3 deposition and $Y(MeCp)_3$ and O_3 for Y_2O_3 deposition. The as-deposited films of CuO were all crystalline as shown by the diffractograms in Fig. 19.

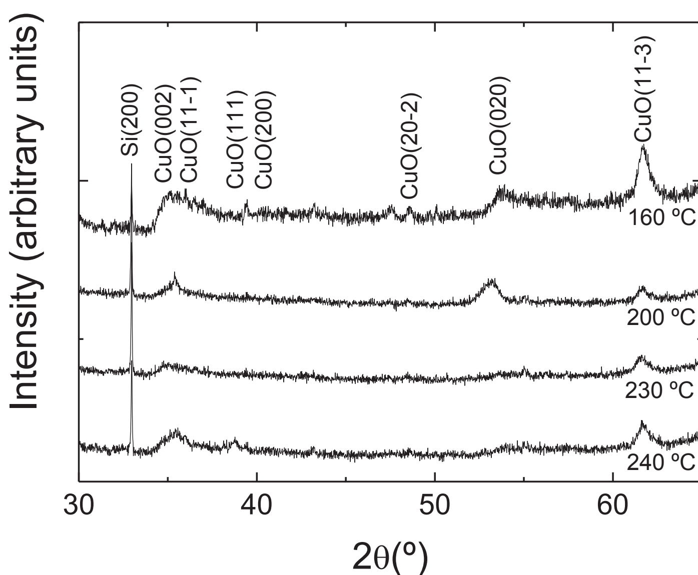

Fig 19 X-ray diffractogram of films deposited on Si(100) substrates at various temperatures with 2500 cycles.

XPS analysis of the as-deposited films were carried out for films deposited at 160, 200 and 230 ºC to analyze the oxidation state of copper on the surface. It was found that the samples only contained Cu^{2+}.

Compared to previous work using copper containing precursors (see Chapter 2.5.3), the $Cu(acac)_2$ and O_3 process seems to be a robust process covering a larger temperature window.

4.3.2 Deposition of Cu-Al-O and Cu-Y-O films

Mixing copper oxide with the known ALD processes for Al_2O_3[26] or Y_2O_3[191] was performed at 200 ºC since all processes work at this temperature. The operational parameters for the processes used are shown in Table 4. Note that SnO_2 was used as a buffer layer for some of the Cu-Al-O films.

Table 4: Materials, precursor combinations, deposition parameters, and obtained growth rate at a deposition temperature of 200 ºC

Material	Precursors/process	Pulse- and purge scheme (s)	Metal precursor temperature (ºC)	Growth rate (nm/cycle)
CuO	$Cu(acac)_2 + O_3$	3-1-3-3	140	0.038
Al_2O_3	$TMA + O_3$	0.2-1-3-5	RT	0.115
Y_2O_3	$Y(MeCp)_3 + H_2O$	3-2-2-4	140	0.15
SnO_2	$SnI_4 + O_3$	3-3-3-3	75	0.17

The first step in obtaining the correct stoichiometry is to vary the pulsing scheme for the binary oxides when mixing the oxides. The series of samples can then be analyzed by XRF. Fig. 20 and Fig. 21 show the mixing of CuO and Al_2O_3 and CuO and Y_2O_3, respectively.

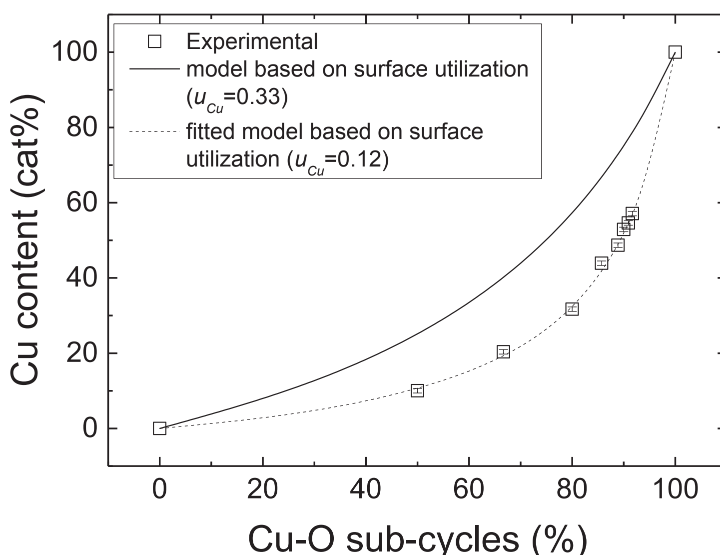

Fig 20 Cationic Cu composition of deposited material as function of % of Cu-O sub-cycles in the [TMA/O_3 + $Cu(acac)_2/O_3$] system (square symbols). The experimental data is compared with a model based on individual growth rates (solid line) and model based on surface utilization[34] optimized with a u-value of 0.12 (dotted line).

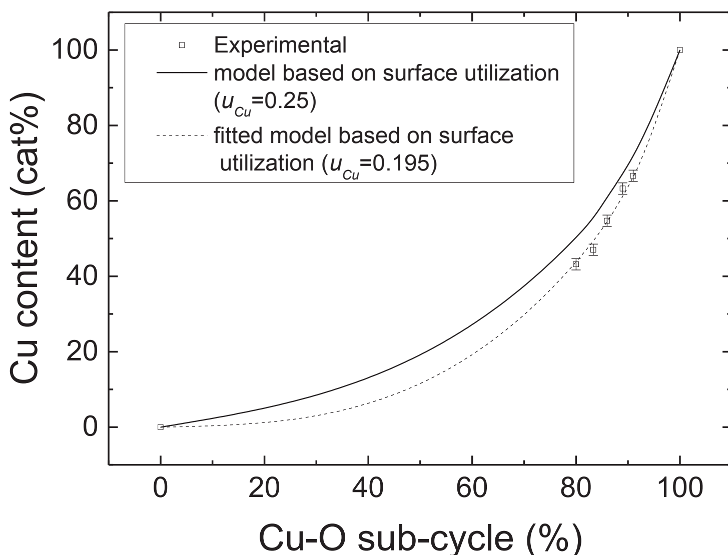

Fig 21 Cationic Cu composition of deposited material as function of % of Cu-O sub-cycles in the [$Y(MeCp)_3/H_2O$ + $Cu(acac)_2/O_3$] system (symbols). The experimental data is compared with a model based on individual growth rates (solid line) and a model based on surface utilization[34] optimized with a u-value of 0.195 (dotted line).

For both systems the surface utilization concept (described in chapter 2.4.1) was used. The model was initially used to predict the correct pulsing ratio between the copper oxide and the aluminum oxide or yttrium oxide. Before fitting the model to the experimentally obtained data it is only based on the individual growth rates of the binary oxides (actual and relative growth rates are given in Table 5). For the mixing of Cu and Al, a pulsing ratio of 3:1 was expected to give equimolar amounts of Cu and Al in the films. For the Cu and Y process, a pulsing ratio of 4:1 was expected. As can be seen in Fig. 20 and Fig. 21 this was not correct. The model was fitted to the experimentally obtained XRF data revealing that a pulsing ratio of 8.3:1 of Cu:Al was required to obtain almost equimolar composition in the film, while for Cu and Y a ratio of 5:1 was sufficient to achieve the correct composition.

Based on these findings it was interesting to look deeper into the growth rates for the systems when the binary processes were combined. The fitted u-value for the systems makes it possible to propose some assumptions on how the processes influence each other.

Fig. 22 shows the thickness of the film as measured by XRR against the Cu-O sub-cycle (%).

Table 5: Calculated and modified u-values based on the XRF data, and new growth rates calculated from the modified u-values. U-values are calculated using Equation (2.5).

System	Binary Oxide	Growth rate (nm/cycle) (XRR)	u-value obtained from individual growth rates[34]	Modified u-values based on XRF data	New growth rate (CuO not changed)	New growth rate (Al_2O_3 not changed)
Cu-Al-O	Al_2O_3	0.115	1	1	0.316	0.115
	CuO	0.038	0.33	0.12	0.038	0.014
Cu-Y-O	Y_2O_3	0.15	1	1	0.195	0.15
	CuO	0.038	0.25	0.195	0.038	0.029

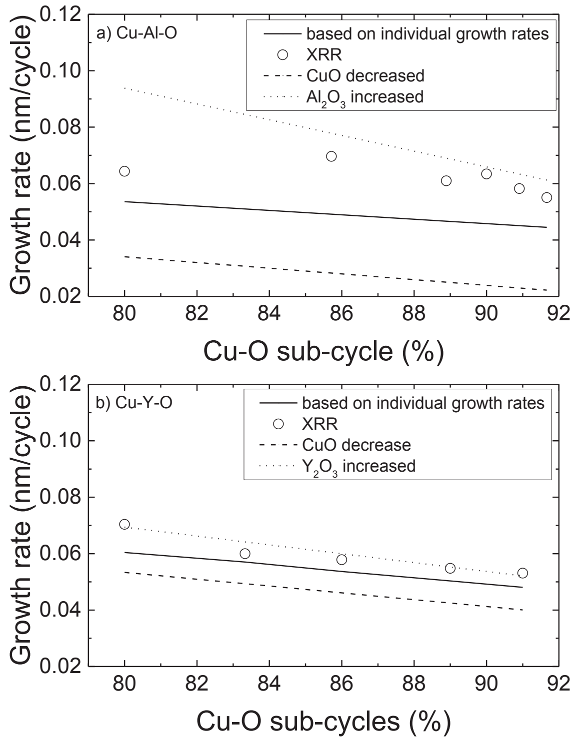

Fig 22 Growth rate as function of % of Cu-O sub-cycles in the a) [TMA/O_3 + Cu(acac)$_2$/O_3] and b) [Y(MeCp)$_3$/H_2O + Cu(acac)$_2$/O_3] systems as measured by XRR (open circles) and compared to a model based on individual growth rates (black solid line). Dashed and dotted lines are based on new growth rates obtained by using the model of surface utilization to fit to the XRF data. Values are given in Table 5.

Together with the actual growth rate measured by XRR, theoretical growth rates are calculated based on the individual growth rates of the binary oxides, and also based on new growth rates from the fitted u-value. As can be seen from Fig. 22 the growth rate of the two systems is higher than what would be expected from the individual growth rates for the binary oxides. The relative growth rate (u_{Cu}) is reduced for both systems. A reduction of u_{Cu} can indicate two things: either the growth rate of CuO is decreased, or the growth rate of Al_2O_3/Y_2O_3 is increased. However, a decrease in the growth rate of CuO while the

growth rate of the other oxide is unchanged would lead to a lower overall growth rate for the system. Therefore it is more likely that the growth rate of Al_2O_3 or Y_2O_3 is increased. An increase in the growth rate of Al_2O_3 and Y_2O_3 when combined with CuO would also explain why a higher Cu-O sub-cycle % is needed to obtain the right composition. This trend is more pronounced for the Cu-Al-O system than for the Cu-Y-O system.

4.3.3 $CuAlO_2$

A Cu-Al-O film with a small surplus of copper was deposited on quartz wool that had been pre-coated with a buffer layer of SnO_2. After deposition the sample was black due to presence of CuO. It was then subsequently annealed in N_2 at 1050 ºC for 4h, changing the color to red due to the conversion of CuO to Cu_2O. The sample was analyzed using SXRD, spectra shown in Fig. 23.

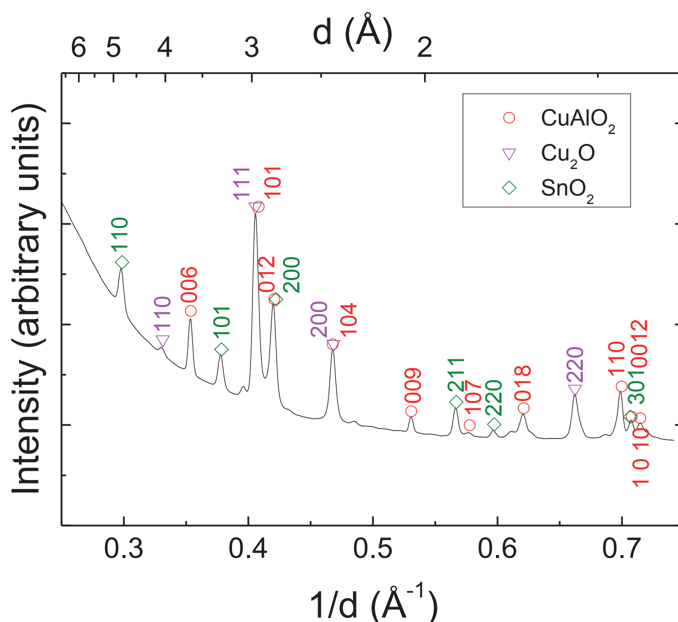

Fig 23 Growth X-ray diffractogram based on synchrotron radiation (λ = 0.6965 Å) of a Cu-Al-O film with composition of 53% Cu and 47% Al (given by XRF) deposited on quartz wool pre-coated with SnO_2. The sample was annealed in N_2 atmosphere for 4h at 1050 ºC, and quenched to room temperature. The phases were identified according to the PDF files: $CuAlO_2$ (35-1401), Cu_2O (5-0667) and SnO_2 (41-1445).

The desired $CuAlO_2$ phase was formed. Another experiment was carried out where the film was deposited on α-Al_2O_3. The diffractogram is shown in Fig. 24. When the film was deposited on α-Al_2O_3 delafossite was again formed. There was, however, a small amount of $CuAl_2O_4$ present in the film (note logarithmic y-scale). This could be due to reaction between the film and the substrate.

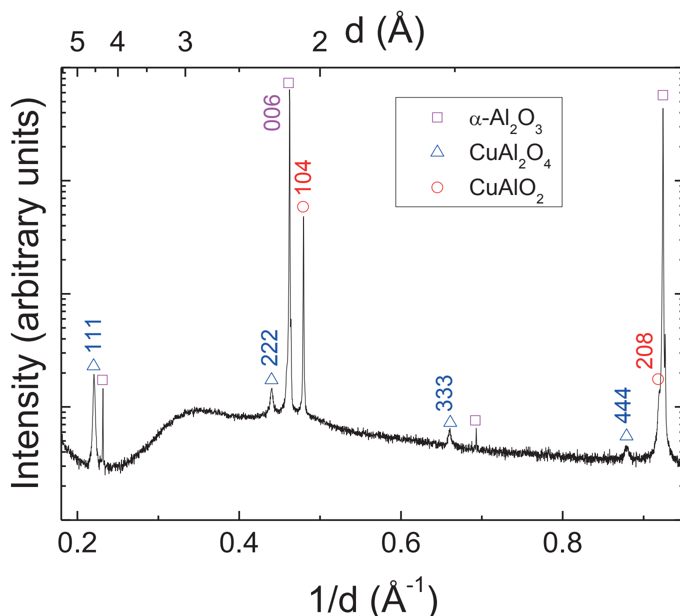

Fig 24 X-ray diffractogram of Cu-Al-O film with composition of 49% Cu and 51 % Al (given by XRF) deposited on α-Al_2O_3(00l) ; note logarithmic scale. The sample is annealed in N_2 for 4 h at 1050 ºC, and quenched to room temperature. The phases were identified according to the PDF files: α-Al_2O_3 (46-1212), $CuAl_2O_4$ (33-0448) and $CuAlO_2$ (35-1401).

Electrical measurements of the $CuAlO_2$ sample deposited on α-Al_2O_3(001) was attempted after annealing, however, the resistivity was too high (> 1 MΩcm) for suitable characterization.

4.3.4 Cu-Y-O

Figure 25 show X-ray diffractograms of Cu-Y-O film deposited on α-Al_2O_3(001). The sample was annealed in N_2 for 4 h at 1025 ºC whereby $YAlO_3$ is formed. It was not possible to identify any copper containing compounds in the observed pattern.

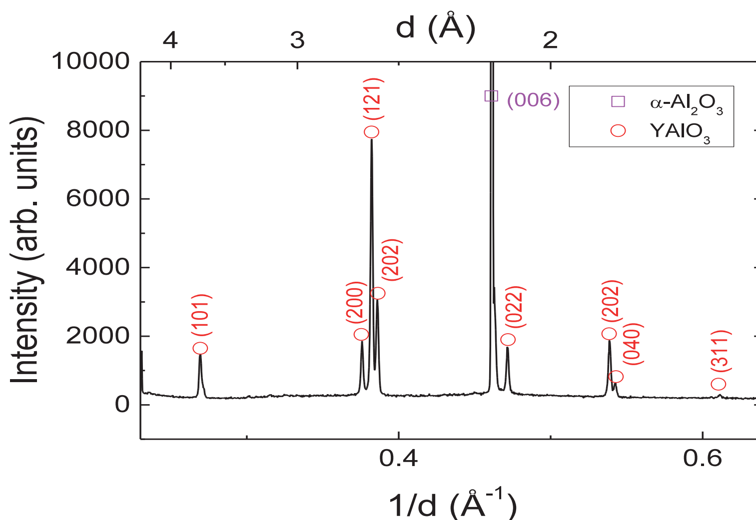

Fig 25 X-ray diffractogram of a Cu-Y-O film with composition 47 cat% Cu and 53 cat% Y (given by XRF) deposited on α-Al_2O_3(001) and annealed in N_2 atmosphere for 4 h at 1025 ºC. The phases were identified using the PDF files: α-Al_2O_3 (46-1212) and $YAlO_3$ (33-0041).

Film deposited with the same composition on other substrates were also annealed and analyzed. However, these experiments did not result in films that gave any recognizable phases when analyzed by XRD.

We were able to make films of $CuAlO_2$ having the delafossite type structure, however, electrical characterization of the films were not possible due to the high resistivity of the films.

5 Concluding remarks and future work

The main focus of this work has been on three TCO materials; ZnO, SnO_2 and especially $CuAlO_2$ with the delafossite type structure.

The work related to deposition of ZnO focus on the precursors used and whether they themselves are a source for impurities in the film, especially with respect to Al content. It was evident that even relatively high purity precursors commercially sold for ALD deposition contain enough Al to lead to significant Al-doping in the deposited films. The level of impurity is not easily controlled if the purity grade of the precursor is not especially high. Related to this work the heterojunction between the film and the Si substrate was studied. This is important if ZnO is to be used as a transparent electrode for solar cells. It was seen that the junction was improved by annealing the film at 400 ºC.

Low temperature deposition of SnO_2 was achieved by reacting SnI_4 and O_3. The lowest deposition temperature was 110 ºC and the resulting films were amorphous below deposition temperatures of 300 ºC. The amorphous films showed poor electrical conductivity while the film deposited at 300 ºC showed specific resistivity of $7.1 \cdot 10^{-3}$ Ω cm, carrier concentration of $5 \cdot 10^{19}$ cm^{-3} and a mobility of 17 $cm^2/V \cdot s$. A deposition temperature of 300 ºC might be too high for some industrial processes.

In order to deposit films in the Cu-*M*-O (*M*=Al or Y) system a process to deposit CuO was studied using copper acetylacetonate, $Cu(acac)_2$, and O_3. This process was found to give uniform films following the self-limiting growth of ALD in a temperature range of 140 – 230 ºC with a growth rate of ~0.038 nm/cycle. The films were crystalline adopting the tenorite structure.

Good control of stoichiometry was achieved when mixing CuO with Al_2O_3 or Y_2O_3. Films having the delafossite oxide type structure were obtained by high temperature annealing of films containing Cu and Al. Electrical measurements were unfortunately not possible due to the low electrical conductivity of these films. The high annealing temperature required would not be suitable for industrial application. However, the good control of

stoichiometry makes the atomic layer deposition process suitable for producing and studying such complex oxides.

For further work it would be interesting to investigate whether it would be possible to induce defects in the $CuAlO_2$ films to enhance the electrical properties. Since ALD is a good technique to deposit complex oxides and TCO materials it would be useful and highly interesting to develop routes to deposit other oxides and oxychalcogenides reported in literature to have p-type conductivity.

In the search for transparent electrodes to either replace ITO or to facilitate new applications there are several possibilities reported in the literature. For n-type TCO's the main focus is still on doping of SnO_2 and ZnO or mixing of the three well-known TCO's SnO_2, ZnO and In_2O_3. Another important oxide system is niobium (Nb) or tantalum (Ta) doped TiO_2[192, 193]. Doped TiO_2 have gained interest due to its chemical stability and low resistivity. The drawback is the high process temperature[193]. Finding a good p-type TCO remains still challenging[12]. Other strategies to create transparent electrodes include multilayered structures with metallic layers in between dielectric oxides[194]. Much attention is also given to graphene, that some say might be the new disruptive technology to replace materials used today[195].

Graphene has outstanding properties such as high conductivity and charge carrier mobility. It has a transparency > 90% and it is chemically inert and has low permeability towards gases. It has a bendability below 5 mm[195, 196]. for typical flexible devices the bendability of the TC material should be below 1.5 cm[194]. The multilayered structures are also good candidates to be used as TC materials on flexible substrates, however, they do tend to have lower transparency[194]. ITO has good transparency and conductive properties that would be advantageous on flexible substrates and on organic based devices. However, the material is brittle and it can degrade in contact with organic materials[194]. For graphene and other technologies to take over for the traditional TCO materials there are several challenges to overcome such as low-cost production and higher material quality[193, 195, 196].

6 References

1. T. F. Stocker, D. Qin, G.-K. Plattner, M. Tignor, S.K. Allen, J. Boschung, A. Nauels, Y. Xia, V. Bex and P.M. Midgley (*IPCC, 2013: Summary for Policymakers. In: Climate Change 2013: The Physical Science Basis. Contribution of Working Group I to the Fifth Assessment Report of the Intergovernmental Panel on Climate Change*, 2013.
2. O. Edenhofer, R. Pichs-Madruga, Y. Sokona, E. Farahani, S. Kadner, K. Seyboth, A. Adler, I. Baum, S. Brunner, P. Eickemeier, B. Kriemann, J. Savolainen, S. Schlömer, C. von Stechow, T. Zwickel and J.C. Minx *IPCC, 2014: Summary for Policymakers, In: Climate Change 2014, Mitigation of Climate Change. Contribution of Working Group III to the Fifth Assessment Report of the Intergovernmental Panel on Climate Change* 2014.
3. The World Fact Book, https://www.cia.gov/library/publications/the-world-factbook/geos/xx.html Accessed 29.07, 2014.
4. D. Arvizu, P. Balaya, L. F. Cabeza, K. G. T. Hollands, A. Jäger-Waldau, M. Kondo, C. Konseibo, V. Meleshko, W. Stein, Y. Tamaura, H. Xu and R. Zilles, in *IPCC Special Report on Renewable Energy Sources and Climate Change Mitigation*, eds. O. Edenhofer, R. Pichs-Madruga, Y. Sokona, K. Seyboth, P. Matschoss, S. Kadner, T. Zwickel, P. Eickemeier, G. Hansen, S. Schlömer and C. von Stechow, Cambridge University Press, Cambridge, United Kingdom and New York, NY, USA, 2011.
5. D. Arvizu, T. Bruckner, H. Chum, O. Edenhofer, S. Estefen, A. Faaij, M. Fischedick, G. Hansen, G. Hiriart, O. Hohmeyer, K. G. T. Hollands, J. Huckerby, S. Kadner, Å. Killingtveit, A. Kumar, A. Lewis, O. Lucon, P. Matschoss, L. Maurice, M. Mirza, C. Mitchell, W. Moomaw, J. Moreira, L. J. Nilsson, J. Nyboer, R. Pichs-Madruga, J. Sathaye, J. L. Sawin, R. Schaeffer, T. A. Schei, S. Schlömer, K. Seyboth, R. Sims, G. Sinden, Y. Sokona, C. v. Stechow, J. Steckel, A. Verbruggen, R. Wiser, F. Yamba and T. Zwickel, in *IPCC Special Report on Renewable Energy Sources and Climate Change Mitigation*, eds. O. Edenhofer, R. Pichs-Madruga, Y. Sokona, K. Seyboth, P. Matschoss, S. Kadner, T. Zwickel, P. Eickemeier, G. Hansen, S. Schlömer and C. von Stechow, Cambridge University Press, Cambridge, United Kingdom and New York, NY, USA, 2011.
6. in *IPCC Special Report on Renewable Energy Sources and Climate Change Mitigation.*, eds. O. Edenhofer, R. Pichs-Madruga, Y. Sokona, K. Seyboth, P. Matschoss, S. Kadner, T. Zwickel, P. Eickemeier, G. Hansen, S. Schlömer and C. von Stechow, Cambridge University Press, Cambridge, United Kingdom and New York, NY, USA, 2011.
7. A. Chipman, *Nature*, 2007, 449, 131.
8. J. M. Crow, *New Sci.* , 2011, 210, 36-41.
9. B. A. Andersson, *Prog. Photovolt: Res. Appl.*, 2000, 8, 61-76.
10. A. Feltrin and A. Freundlich, *Renew. Energ.*, 2008, 33, 180-185.
11. J. F. Wager, D. A. Keszler and R. E. Presley, *Transparent Electronics*, Springer Science+Business Media, LLC, Boston, MA, 2008.
12. T. Minami, in *Semiconductors and Semimetals*, eds. S. J. P. Bengt G. Svensson and J. Chennupati, Elsevier, 2013, vol. Volume 88, pp. 159-200.
13. R. J. D. Tilley, *Understanding solids: the science of materials*, Wiley, Chichester, 2004.

14. J. Robertson, K. Xiong and S. J. Clark, *Thin Solid Films*, 2006, 496, 1-7.
15. M. Mohamed, Wikimedia Commons, http://commons.wikimedia.org/wiki/File:Wiki_mc_fig45.PNG?uselang=nb, Accessed 13.08, 2014.
16. R. Hoffmann, *Solids and Surfaces: A Chemist*s View of Bonding in Extended Structures* VCH Publishers, Inc., New York, 1988.
17. P. Y. Yu and M. Cardona, *Fundamentals of Semiconductors: Physics and Materials Properties, 3rd Edition*, Springer-Verlag, 2001.
18. P.-A. Hansen, Department of Chemistry, Faculty of Mathematics and Natural Sciences, University of Oslo, 2014.
19. D. S. Ginley, H. Hosono and D. P. Paine, *Handbook of transparent conductors*, Springer, New York, 2010.
20. A. Zunger, *Appl. Phys. Lett*, 2003, 83, 57-59.
21. C. E. Corporation, Array of solar panels, http://www.products.cvdequipment.com/applications/1/, Accessed 28.08, 2014.
22. Jin-Suk Seo, Jun-Hyuck Jeon, Young Hwan Hwang, Hyungjin Park, Minki Ryu, Sang-Hee Ko Park and B.-S. Bae, Figure 3: Characterization of flexible IZO:F TFT on PEN film annealed at 200°C., http://www.nature.com/srep/2013/130627/srep02085/fig_tab/srep02085_F3.html, Accessed 28.08, 2014.
23. Oxide electronics: Transparent success, http://www.nature.com/am/journal/2009/200903/full/am200993a.html, Accessed 28.08, 2014.
24. C. G. Granqvist, *Sol. Energy Mater. Sol. Cells*, 2007, 91, 1529-1598.
25. V. Miikkulainen, *J. Appl. Phys.*, 2013, 113, 021301-021101.
26. R. L. Puurunen, *J.Appl. Phys.*, 2005, 97, 121301-121352.
27. V. Miikkulainen, PhD, University of Eastern Finland
2008.
28. M. Ritala, *ECS transactions*, 2009, 25, 641-652.
29. D. Levy, S. Freeman, P. Nelson, L. Cowdery Corvan and Irving, *Appl. Phys. Lett*, 2008, 92, 192101-192103.
30. T. Suntola, *Thin Solid Films*, 1992, 216, 84-89.
31. *Finland Pat.,* U.S. Patent No. 4058430, 1977.
32. T. Suntola and J. Hyvärinen, *Annu. Rev. Mater. Sci.*, 1985, 15, 177-195.
33. M. Ylilammi, *Thin Solid Films*, 1996, 279, 124-130.
34. O. Nilsen, M. Lie, H. F. Fjellvåg and A. Kjekshus, *Top. Appl. Phys.*, 2007, 106, 87-99.
35. M. Nieminen, S. Lehto and L. Niinistoe, *J. Mater. Chem.*, 2001, 11, 3148-3153.
36. M. Nieminen, T. Sajavaara, E. Rauhala, M. Putkonen and L. Niinistoe, *J. Mater. Chem.*, 2001, 11, 2340-2345.
37. J. Harjuoja, A. Kosola, M. Putkonen and L. Niinistö, *Thin Solid Films*, 2006, 496, 346-352.
38. M. Putkonen, T. Sajavaara, J. Niinisto, L.-S. Johansson and L. Niinisto, *J. Mater. Chem.*, 2002, 12, 442-448.
39. K. Baedeker, *Ann. Phys. (Weinheim, Ger.)*, 1907, 22, 749-766.
40. T. Minami and T. Miyata, *Thin Solid Films*, 2008, 517, 1474-1477.
41. K. Ellmer, *J. Phys. D: Appl. Phys*, 2001, 34, 3097-3108.
42. P. D. King, *J. Phys.: Condens. Matter*, 2011, 23, 334214-334217.
43. Y. Kajikawa, *J. Cryst. Growth*, 2006, 289, 387-394.

44. R. Triboulet and J. Perrière, *Prog. Cryst. Growth Charact. Mater.*, 2003, 47, 65-138.
45. K. Ellmer, A. Klein, B. Rech and Editors, *Transparent conductive zinc oxide: basics and applications in thin film solar cells. [In: Springer Ser. Mater. Sci., 2008; 104]*, Springer, 2008.
46. W. Park, *Met. Mater. Int.*, 2008, 14, 659-665.
47. T. Tynell, *Semicond. Sci. Technol.*, 2014, 29, 043001-043015.
48. H. Agura, A. Suzuki, T. Matsushita, T. Aoki and M. Okuda, *Thin Solid Films*, 2003, 445, 263-267.
49. A. Rosental, A. Tarre, A. Gerst, J. Sundqvist, A. Hårsta, A. Aidla, J. Aarik, V. Sammelselg and T. Uustare, *Sensor Actuat. B-Chem*, 2003, 93, 552-555.
50. V. Aravindan, K. B. Jinesh, R. R. Prabhakar, V. S. Kale and S. Madhavi, *Nano Energy*, 2013, 2, 720-725.
51. J.-H. Jeun, K.-Y. Park, D.-H. Kim, W.-S. Kim, H.-C. Kim, B.-S. Lee, W.-R. Yu, K. Kang and S.-H. Hong, *Nanoscale*, 2013, 5, 8480-8483.
52. H. Viirola and L. Niinistö, *Thin Solid Films*, 1994, 251, 127-135.
53. J. W. Elam, D. A. Baker, A. B. F. Martinson, M. J. Pellin and J. T. Hupp, *J. Phys. Chem. C*, 2008, 112, 1938-1945.
54. C. Prasittichai, J. Prasittichai and Hupp, *J. Phys. Chem. Lett.* , 2010, 1, 1611-1615.
55. T. Minami, *Semicond. Sci. Technol.*, 2005, 20, S35-S44.
56. T. Ishida, O. Tabata, J. i. Park, S. H. Shin, H. Magara, S. Tamura, S. Mochizuki and T. Mihara, *Thin Solid Films*, 1996, 281–282, 228-231.
57. K. G. Godinho, A. Walsh and G. W. Watson, *J. Phys. Chem. C.*, 2008, 113, 439-448.
58. M. Batzill and U. Diebold, *Prog. surf. sci.* , 2005, 79, 47-154.
59. R. Matero, A. Rahtu, M. Ritala, M. Leskelä and T. Sajavaara, *Thin Solid Films*, 2000, 368, 1-7.
60. A. Tarre, A. Rosental, V. Sammelselg and T. Uustare, *Appl. Surf. Sci.*, 2001, 175–176, 111-116.
61. M. Utriainen, S. Lehto, L. Niinistö, C. Dücső, N. Q. Khanh, Z. E. Horváth, I. Bársony and B. Pécz, *Thin Solid Films*, 1997, 297, 39-42.
62. H. Viirola and L. Niinistö, *Thin Solid Films*, 1994, 249, 144-149.
63. R. R. Rachkovskii, S. I. Kol'tsov and V. B. Aleskovskii, *Zh. Neorg. Khim.*, 1970, 15, 3158.
64. V. Smirnov, *J. Appl. Chem-USSR+*, 1992, 65, 2666.
65. C. Ducso, N. Q. Khanh, Z. Horvath, I. Barsony and M. Utriainen, *J. Electrochem. Soc.*, 1996, 143, 683-687.
66. M. Utriainen, K. Kovacs, J. M. Campbell, L. Niinisto and F. Reti, *J. Electrochem. Soc.*, 1999, 146, 189-193.
67. M. Utriainen, L. Niinisto and R. Matero, *Appl. Phys. A: Mater. Sci. Process.*, 1999, 68, 339-342.
68. M. Utriainen, H. Lattu, H. Viirola, L. Niinisto, R. Resch and G. Friedbacher, *Mikrochim. Acta*, 2000, 133, 119-123.
69. A. Rosental, A. Tarre, A. Gerst, T. Uustare and V. Sammelselg, *Sensor. Actuat. B-Chem.*, 2001, 77, 297-300.
70. J. Lu, J. Sundqvist, M. Ottosson, A. Tarre, A. Rosental, J. Aarik and A. Hårsta, *J. Cryst. Growth*, 2004, 260, 191-200.
71. X. Meng, Y. Zhang, S. Sun, R. Li and X. Sun, *J. Mater. Chem.*, 2011, 21, 12321-12330.

72. X. Meng, Y. Zhong, Y. Sun, M. N. Banis, R. Li and X. Sun, *Carbon*, 2011, 49, 1133-1144.
73. H.-E. Cheng, D.-C. Tian and K.-C. Huang, *Procedia Engineering*, 2012, 36, 510-515.
74. Y. Chen, J. Wang, X. Meng, Y. Zhong, R. Li, X. Sun, S. Ye and S. Knights, *J. Power Sources*, 2013, 238, 144-149.
75. F. Grote, L. Wen and Y. Lei, *J. Power Sources*, 2014, 256, 37-42.
76. S. Park, S. An, C. Jin and C. Lee, *J. Korean Phys. Soc.*, 2012, 61, 843-846.
77. X. Li, X. Meng, J. Liu, D. Geng, Y. Zhang, M. N. Banis, Y. Li, J. Yang, R. Li, X. Sun, M. Cai and M. W. Verbrugge, *Adv. Funct. Mater.*, 2012, 22, 1647-1654.
78. C. Jin, H. Kim, C. Hong, S. Park and C. Lee, *Mater. Lett.*, 2011, 65, 3275-3277.
79. Y. Chen, J. Wang, X. Meng, Y. Zhong, R. Li, X. Sun, S. Ye and S. Knights, *Int. J. Hydrogen Energ.*, 2011, 36, 11085-11092.
80. C. Jin, H. Kim, H.-Y. Ryu, H. W. Kim and C. Lee, *J. Phys. Chem. C.*, 2011, 115, 8513-8518.
81. M. Ritala, M. Leskela and T. Asikainen, *J. Electrochem. Soc.*, 1995, 142, 3538-3541.
82. A. Tarre, A. Rosental, A. Aidla, J. Aarik, J. Sundqvist and A. Hårsta, *Vacuum*, 2002, 67, 571-575.
83. J. D. Ferguson, K. J. Buechler, A. W. Weimer and S. M. George, *Powder Technol.*, 2005, 156, 154-163.
84. X. Du, Y. Du and S. M. George, *J. Vac. Sci. Technol., A*, 2005, 23, 581-588.
85. X. Du and S. M. George, *Sensor Actuat. B-Chem*, 2008, 135, 152-160.
86. X. Du, Y. Du and S. M. George, *J. Phys. Chem. A*, 2008, 112, 9211-9219.
87. A. Tarre, A. Rosental, J. Sundqvist, A. Hårsta, T. Uustare and V. Sammelselg, *Surf. Sci* 2003, 532–535, 514-518.
88. J. Sundqvist, A. Tarre, A. Rosental and A. Hårsta, *Chem. Vap. Deposition*, 2003, 9, 21-25.
89. J. Sundqvist, J. Lu, M. Ottosson and A. Hårsta, *Thin Solid Films*, 2006, 514, 63-68.
90. A. Rosental, A. Tarre, A. Gerst, A. Kasikov and J. Lu, *IEEE Sens. J.*, 2013, 13, 1648-1655.
91. V. E. Drozd and V. B. Aleskovski, *Appl. Surf. Sci.*, 1994, 82–83, 591-594.
92. H.-T. Wang, S. Xu and R. Gordon, *Electrochem. Solid. St.*, 2010, 13, G75.
93. W. Lee, *J. Korean Phys. Soc.*, 2005, 46, L756-L759.
94. G. Choi, L. Satyanarayana and J. Park, *Appl. Surf. Sci.*, 2006, 252, 7878-7883.
95. W.-S. Kim, *Nanotechnology*, 2010, 21, 245605-245607.
96. D. Kim, W.-S. Kim, S. Lee and S.-H. Hong, *Sensor Actuat. B-Chem*, 2010, 147, 653-659.
97. D. H. Kim, J.-H. Kwon, M. Kim and S.-H. Hong, *J. Cryst. Growth*, 2011, 322, 33-37.
98. S. Kim, D.-H. Kim and S.-H. Hong, *J. Cryst. Growth*, 2012, 348, 15-19.
99. B.-S. Lee, W.-S. Kim, D.-H. Kim, H.-C. Kim, S.-H. Hong and W.-R. Yu, *Smart. Mater. Struc.*, 2011, 20, 105019-105017.
100. Y.-G. Jang, W.-S. Kim, D.-H. Kim and S.-H. Hong, *Journal of Materials Research*, 2011, 26, 2322-2327.
101. J. W. Elam, D. A. Baker, A. J. Hryn, A. B. F. Martinson, M. J. Pellin and J. T. Hupp, *J. Vac. Sci. Technol., A*, 2008, 26, 244-252.
102. M. Stefik, M. Cornuz, N. Mathews, T. Hisatomi, S. Mhaisalkar and M. GrÃ¤tzel, *Nano Lett.* , 2012, 12, 5431-5435.

103. M. N. Mullings, C. Hägglund and S. F. Bent, *J. Vac. Sci. Technol., A*, 2013, 31, 061503-061508.
104. J. Haag, G. Pattanaik and M. Durstock, *Adv. Mater.*, 2013, 25, 3238-3243.
105. M. Kapilashrami, C. X. Kronawitter, T. Torndahl, J. Lindahl, A. Hultqvist, W.-C. Wang, C.-L. Chang, S. S. Mao and J. Guo, *Phys. Chem. Chem. Phys.*, 2012, 14, 10154-10159.
106. J. T. Tanskanen, C. Hägglund and S. F. Bent, *Chem. Mater.*, 2014, 26, 2795-2802.
107. M. N. Mullings, C. Hägglund, J. T. Tanskanen, Y. Yee, S. Geyer and S. F. Bent, *Thin Solid Films*, 2014, 556, 186-194.
108. J. Heo, A. S. Hock and R. G. Gordon, *Chem. Mater.*, 2010, 22, 4964-4973.
109. J. Heo, Y. Liu, P. Sinsermsuksakul, Z. Li, L. Sun, W. Noh and R. G. Gordon, *J. Phys. Chem. C*, 2011, 115, 10277-10283.
110. J. Heo, S. Bok Kim and R. G. Gordon, *Appl. Phys. Lett*, 2012, 101, 113507-113505.
111. J. Heo, S. B. Kim and R. G. Gordon, *J. Mater. Chem.*, 2012, 22, 4599-4602.
112. C. Marichy, N. Donato, M.-G. Willinger, M. Latino, D. Karpinsky, S.-H. Yu, G. Neri and N. Pinna, *Adv. Funct. Mater.*, 2011, 21, 658-666.
113. C. Marichy, *J. Phys. Chem. C*, 2013, 117, 19729-19739.
114. B. K. Lee, E. Jung, S. H. Kim, D. C. Moon, S. S. Lee, B. K. Park, J. H. Hwang, T.-M. Chung, C. G. Kim and K.-S. An, *Mater. Res. Bull.*, 2012, 47, 3052-3055.
115. S. Kannan Selvaraj, A. Feinerman and C. G. Takoudis, *J. Vac. Sci. Technol., A*, 2014, 32, 01A112-116.
116. S. Haukka, E. L. Lakomaa and T. Suntola, *Studies in Surface Science and Catalysis*, 1999, 120A, 715-750.
117. S. Hüfner, M. A. Hossain, A. Damascelli and G. A. Sawatzky, *Reports on Progress in Physics*, 2008, 71, 062501/062501-062501/062509.
118. M. S. Wagh, L. A. Patil, T. Seth and D. P. Amalnerkar, *Materials Chemistry and Physics*, 2004, 84, 228-233.
119. H. Hosono, *Thin Solid Films* 2007, 515, 6000-6014.
120. K. Akimoto, S. Ishizuka, M. Yanagita, Y. Nawa, G. K. Paul and T. Sakurai, *Sol. Energy*, 2006, 80, 715-722.
121. R. D. Schmidt-Whitley, M. Martinez-Clemente and A. Revcolevschi, *J. Cryst. Growth*, 1974, 23, 113-120.
122. L. C. Olsen and R. C. Bohara, *Conference Record of the IEEE Photovoltaic Specialists Conference*, 1975, 11, 381-390.
123. B. P. Rai, *Solar Cells*, 1988, 25, 265-272.
124. M. H. P. Reddy, P. N. Reddy and S. Uthanna, *Indian. J. Pure. Appl. Phys.*, 2010, 48, 420.
125. W. H. Brattain, *Rev. Mod. Phys.*, 1951, 23, 203-212.
126. L. O. Grondahl, *Rev. Mod. Phys.*, 1933, 5, 141-168.
127. Q. B. Zhang, K. L. Zhang, D. G. Xu, G. C. Yang, H. Huang, F. D. Nie, C. M. Liu and S. H. Yang, *Prog. Mater Sci.*, 2014, 60, 208-337.
128. GB260945, 1925.
129. B. K. Meyer, A. Polity, D. Reppin, M. Becker, P. Hering, P. J. Klar, T. Sander, C. Reindl, J. Benz, M. Eickhoff, C. Heiliger, M. Heinemann, J. Blasing, A. Krost, S. Shokovets, C. Muller and C. Ronning, *Phys. Status Solidi B*, 2012, 249, 1487-1509.
130. T. Törndahl, PhD Dissertation, Uppsala Universitet, 2004.
131. T. Waechtler, S. Oswald, N. Roth, A. Jakob, H. Lang, R. Ecke, S. E. Schulz, T. Gessner, A. Moskvinova, S. Schulze and M. Hietschold, *J. Electrochem. Soc.*, 2009, 156, H453-H459.
132. S. Haukka and T. Suntola, *Interface Sci.*, 1997, 5, 119-128.

133. A. M. Molenbroek, S. Haukka and B. S. Clausen, *Journal of Physical Chemistry B*, 1998, 102, 10680-10689.
134. G. Wang, G. Ran, G. Wan, P. Yang, Z. Gao, S. Lin, C. Fu and Y. Qin, *ACS Nano*, 2014, 8, 5330-5338.
135. T. Törndahl, M. Ottosson and J.-O. Carlsson, *Thin Solid Films*, 2004, 458, 129-136.
136. K. Uwai, *J. Cryst. Growth*, 1991, 112, 298-301.
137. M. Melzer, T. Waechtler, S. Müller, H. Fiedler, S. Hermann, R. D. Rodriguez, A. Villabona, A. Sendzik, R. Mothes, S. E. Schulz, D. R. T. Zahn, M. Hietschold, H. Lang and T. Gessner, *Microelectron. Eng.*, 2013, 107, 223-228.
138. G. Salvan, P. Robaschik, M. Fronk, S. Müller, T. Waechtler, S. E. Schulz, R. Mothes, H. Lang, C. Schubert, S. Thomas, M. Albrecht and D. R. T. Zahn, *Microelectron. Eng.*, 2013, 107, 130-133.
139. M. Utriainen, M. Kröger-Laukkanen, L. S. Johansson and L. Niinistö, *Appl. Surf. Sci.*, 2000, 157, 151-158.
140. R. G. van Welzenis, R. A. M. Bink and H. H. Brongersma, *Appl. Surf. Sci.*, 1996, 107, 255-259.
141. J.-D. Kwon, S.-H. Kwon, T.-H. Jung, K.-S. Nam, K.-B. Chung, D.-H. Kim and J.-S. Park, *Appl. Surf. Sci.*, 2013, 285, Part B, 373-379.
142. A. T. Marin, D. Muñoz-Rojas, D. C. Iza, T. Gershon, K. P. Musselman and J. L. MacManus-Driscoll, *Adv. Funct. Mater.*, 2013, 23, 3413-3419.
143. D. Muñoz-Rojas, M. Jordan, C. Yeoh, A. T. Marin, A. Kursumovic, L. A. Dunlop, D. C. Iza, A. Chen, H. Wang and J. L. MacManus Driscoll, *AIP Advances*, 2012, 2, 042179-042177.
144. A. N. Banerjee and K. K. Chattopadhyay, *Prog. Cryst. Growth Charact. Mater.*, 2006, 50, 52.
145. S. Sheng, G. Fang, C. Li, S. Xu and X. Zhao, *Phys. Status Solidi A*, 2006, 203, 1891-1900.
146. Y. K. Jeong and G. M. Choi, *J. Phys. Chem. Solids*, 1996, 57, 81-84.
147. H. Sato, T. Minami, S. Takata and T. Yamada, *Thin Solid Films*, 1993, 236, 27-31.
148. B. Dhandapani and S. T. Oyama, *Appl. Catal. B.*, 1997, 11, 129-166.
149. B. U. Köhler and M. Jansen, *Z. Anorg. Allg. Chem.* , 1986, 543, 73-80.
150. M. N. Huda, Y. Yan, A. Walsh, S.-H. Wei and M. M. Al-Jassim, *Physical Review B: Condensed Matter and Materials Physics*, 2009, 80, 035205/035201-035205/035207.
151. R. D. Shannon, D. B. Rogers and C. T. Prewitt, *Inorg. Chem. FIELD Full Journal Title:Inorganic Chemistry*, 1971, 10, 713-718.
152. A. N. Banerjee and K. K. Chattopadhyay, *Springer Ser. Mater. Sci.*, 2008, 109, 413-484.
153. D. O. Scanlon, K. G. Godinho, B. J. Morgan and G. W. Watson, *J. Chem. Phys.*, 2010, 132, 024707-024710.
154. I. Hamada and H. Katayama-Yoshida, *Physica B*, 2006, 376–377, 808-811.
155. S. A. Mary, B. G. Nair, J. Naduvath, G. S. Okram, S. K. Remillard, P. V. Sreenivasan and R. R. Philip, *J. Alloys. Compd.*, 2014, 600, 159-161.
156. H. Yanagi, T. Hase, S. Ibuki, K. Ueda and H. Hosono, *Appl. Phys. Lett.* , 2001, 78, 1583-1585.
157. M. Singh and B. R. Mehta, *Appl. Phys. Lett*, 2008, 93, 192104-192103.
158. C. W. Teplin, T. Kaydanova, D. L. Young, J. D. Perkins, D. S. Ginley, A. Ode and D. W. Readey, *Appl. Phys. Lett*, 2004, 85, 3789- 3791.
159. H. Yanagi, S.-i. Inoue, K. Ueda, H. Kawazoe, H. Hosono and N. Hamada, *J. Appl. Phys.*, 2000, 88, 4159-4163.

160. K. Ueda, T. Hase, H. Yanagi, H. Kawazoe, H. Hosono, H. Ohta, M. Orita and M. Hirano, *J. Appl. Phys.*, 2001, 89, 1790-1793.
161. R. Nagarajan, A. D. Draeseke, A. W. Sleight and J. Tate, *J. Appl. Phys.*, 2001, 89, 8022-8025.
162. R. Nagarajan, N. Duan, M. K. Jayaraj, J. Li, K. A. Vanaja, A. Yokochi, A. Draeseke, J. Tate and A. W. Sleight, *J. Int. Inorg. Mater.*, 2001, 3, 265-270.
163. M. K. Jayaraj, A. D. Draeseke, J. Tate and A. W. Sleight, *Thin Solid Films*, 2001, 397, 244-248.
164. S. Saadi, A. Bouguelia, A. Derbal and M. Trari, *J. Photochem. Photobiol. A*, 2007, 187, 97-104.
165. M. Younsi, S. Saadi, A. Bouguelia, A. Aider and M. Trari, *Sol. Energy Mater. Sol. Cells*, 2007, 91, 1102-1109.
166. S. Kato, R. Fujimaki, M. Ogasawara, T. Wakabayashi, Y. Nakahara and S. Nakata, *Appl. Catal. B*, 2009, 89, 183-188.
167. K. L. Deutsch and B. H. Shanks, *Appl. Catal., A*, 2014, 470, 390-397.
168. T. Kimura, J. C. Lashley and A. P. Ramirez, *Phys. Rev. B: Condens. Matter Mater. Phys.*, 2006, 73, 220401-220404.
169. Z. Deng, X. Fang, D. Li, S. Zhou, R. Tao, W. Dong, T. Wang, G. Meng and X. Zhu, *J. Alloys. Compd.*, 2009, 484, 619-621.
170. B. J. Ingram, B. J. Harder, N. W. Hrabe, T. O. Mason and K. R. Poeppelmeier, *Chem. Mater.*, 2004, 16, 5623-5629.
171. H. Kawazoe, M. Yasukawa, H. Kyodo, M. Kurita, H. Yanagi and H. Hosono, *Nature*, 1997, 389, 939-942.
172. T. Ishiguro, N. Ishizawa, N. Mizutani and M. Kato, *Journal of Solid State Chemistry*, 1983, 49, 232-236.
173. S. K. Misra and A. C. D. Chaklader, *J. Am. Ceram. Soc.*, 1963, 46, 509.
174. H. Gong, Y. Wang and Y. Luo, *Appl. Phys. Lett.*, 2000, 76, 3959-3961.
175. N. Tsuboi, Y. Takahashi, S. Kobayashi, H. Shimizu, K. Kato and F. Kaneko, *J. Phys. Chem. Solids*, 2003, 64, 1671-1674.
176. G. Dong, M. Zhang, W. Lan, P. Dong and H. Yan, *Vacuum*, 2008, 82, 1321-1324.
177. M. Ohashi, Y. Iida and H. Morikawa, *J. Am. Ceram. Soc.*, 2002, 85, 270-272.
178. K. Tonooka, K. Shimokawa and O. Nishimura, *Thin Solid Films*, 2002, 411, 129-133.
179. A. Gadalla and P. Kongkachuichay, *Journal of Materials Research*, 1991, 6, 450-454.
180. P. E. J. Flewitt and R. K. Wild, *Physical methods for materials characterisation*, Institute of Physics Publ., Bristol, 2003.
181. M. Birkholz, *Thin Film Analysis by X-Ray Scattering*, Wiley-VCH Verlag GmbH & Co. KGaA, Weinheim, 2006.
182. UniQuant, Omega Data Systems, N-5505 Veldhoven, The Netherlands, 1994.
183. S. Kasap, P. Capper and Editors, *Springer Handbook of Electronic and Photonic Materials*, Springer, 2006.
184. Four point probe, http://four-point-probes.com/four-point-probe-manual/, Accessed 23.08, 2014.
185. R. García and R. Pérez, *Surf. Sci. Rep.*, 2002, 47, 197-301.
186. V. Quemener, M. Alnes, L. Vines, P. Rauwel, O. Nilsen, H. Fjellvaag, E. V. Monakhov and B. G. Svensson, *J. Phys. D. Appl. Phys.*, 2012, 45, 315101-315105.
187. V. Quemener, M. Alnes, L. Vines, O. Nilsen, H. Fjellvaag, E. Monakhov, B. Svensson and Svensson, *Diffus. De. B*, 2011, 178-179, 130-135.

188. K. Bergum, No. 1571, Department of Chemistry, Faculty of Mathematics and Natural Sciences, University of Oslo, 2014.
189. S. J. Lim, S. Kwon and H. Kim, *Thin Solid Films*, 2008, 516, 1523-1528.
190. A. Tarre, A. Aidla, H. Mändar, J. Asari, T. Uustare and A. Rosental, Hamburg, Germany, 2010.
191. J. Niinistö, M. Putkonen and L. Niinistö, *Chem. Mater.*, 2004, 16, 2953-2958.
192. C. G. Granqvist, *Thin Solid Films*, 2014, 564, 1-38.
193. K. Ellmer, *Nat. Photonics.*, 2012, 6, 809-817.
194. L. Cattin, J. C. Bernède and M. Morsli, *Phys. Status Solidi A*, 2013, 210, 1047-1061.
195. K. S. Novoselov, V. I. Falko, L. Colombo, P. R. Gellert, M. G. Schwab and K. Kim, *Nature*, 2012, 490, 192-200.
196. K. Rana, J. Singh and J.-H. Ahn, *J. Mater. Chem. C*, 2014, 2, 2646-2656.